iScience

CellPress
OPEN ACCESS

Article

Acute kidney injury leading to CKD is associated with a persistence of metabolic dysfunction and hypertriglyceridemia

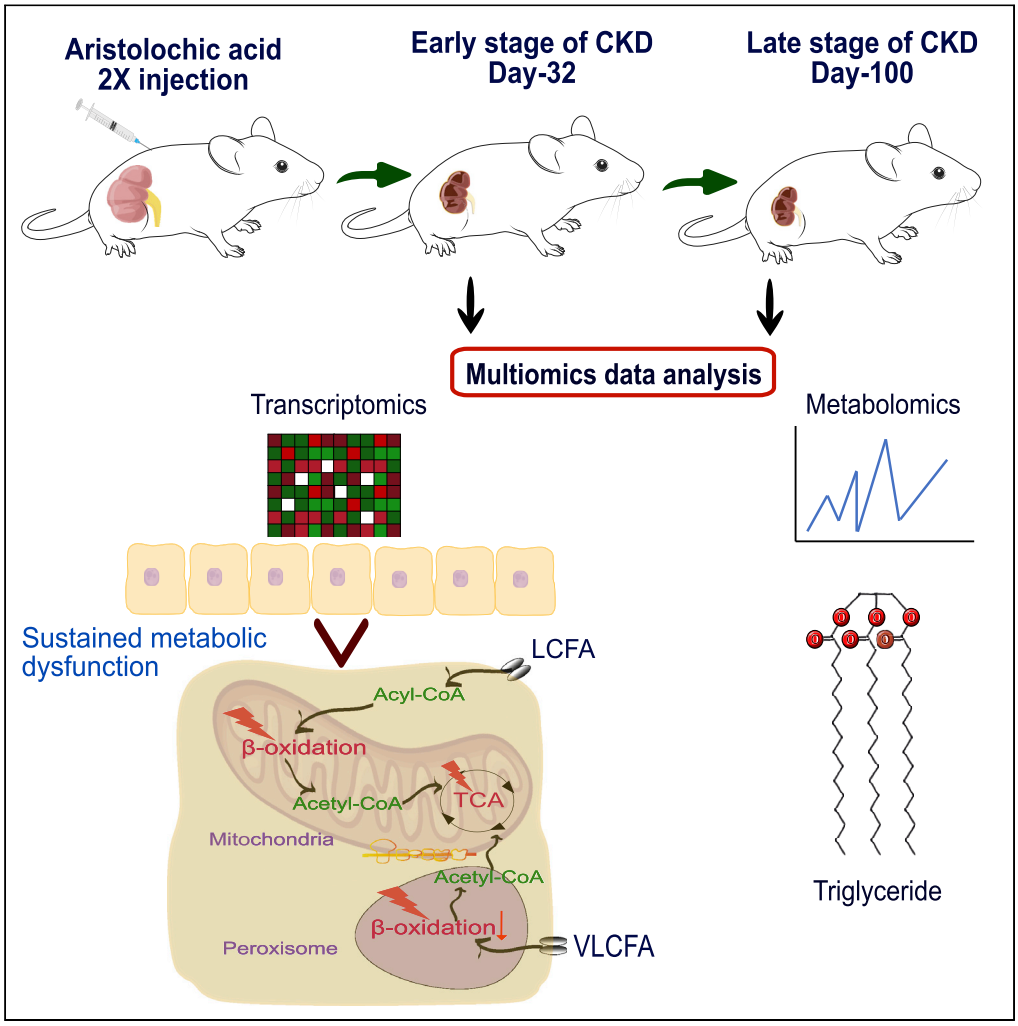

Azadeh Harzandi, Sunjae Lee, Gholamreza Bidkhori, ..., Adil Mardinoglu, Saeed Shoaie, Claire C. Sharpe

adilm@scilifelab.se (A.M.)
saeed.shoaie@kcl.ac.uk (S.S.)
claire.sharpe@kcl.ac.uk (C.C.S.)

HIGHLIGHTS

Following AKI, markers of fibrosis and inflammation go up simultaneously

AKI is associated with reduced fatty acid oxidation and oxidative phosphorylation

Changes in metabolism persist as chronic kidney disease develops

Changes in metabolism are associated with increased serum levels of triglycerides

Harzandi et al., iScience 24, 102046
February 19, 2021
https://doi.org/10.1016/j.isci.2021.102046

iScience

CellPress
OPEN ACCESS

Article

Acute kidney injury leading to CKD is associated with a persistence of metabolic dysfunction and hypertriglyceridemia

Azadeh Harzandi,[1] Sunjae Lee,[2,3] Gholamreza Bidkhori,[3] Sujit Saha,[1] Bruce M. Hendry,[1] Adil Mardinoglu,[3,4,*] Saeed Shoaie,[3,4,*] and Claire C. Sharpe[1,5,*]

SUMMARY

Fibrosis is the pathophysiological hallmark of progressive chronic kidney disease (CKD). The kidney is a highly metabolically active organ, and it has been suggested that disruption in its metabolism leads to renal fibrosis. We developed a longitudinal mouse model of acute kidney injury leading to CKD and an *in vitro* model of epithelial to mesenchymal transition to study changes in metabolism, inflammation, and fibrosis. Using transcriptomics, metabolic modeling, and serum metabolomics, we observed sustained fatty acid metabolic dysfunction in the mouse model from early to late stages of CKD. Increased fatty acid biosynthesis and downregulation of catabolic pathways for triglycerides and diacylglycerides were associated with a marked increase in these lipids in the serum. We therefore suggest that the kidney may be the source of the abnormal lipid profile seen in patients with CKD, which may provide insights into the association between CKD and cardiovascular disease.

INTRODUCTION

The Institute for Health Metrics and Evaluation's Global Burden of Disease Study 2017 highlighted that chronic kidney disease (CKD) is predicted to rise from the 16th (in 2016) to the 5th most common cause of death worldwide by 2040, overtaking diabetes (Jadot et al., 2017).

Since the discovery many decades ago that inhibitors of the renin-angiotensin-aldosterone system could slow the progression of CKD, there has, until recently, been no new disease-modifying drug that preserves kidney function in patients with CKD. Over the past 3 years, however, two new classes of drugs, sodium-glucose linked transporter protein 2 (SGLT2) inhibitors and non-steroidal, selective mineralocorticoid receptor antagonists have been shown in clinical trials to preserve kidney function in patients with progressive CKD with (and in the case of dapagliflozin without) type 2 diabetes (Bakris et al., 2020; Heerspink et al., 2020; Perkovic et al., 2019). These exciting trials have demonstrated that this hitherto predicted epidemic of CKD can be averted with new therapeutic interventions. Furthermore, we suggest that a better understanding of the complex mechanisms that drive this disease may lead to the development of many more drugs for use in preventing or slowing CKD.

CKD is defined as the progressive and irreversible loss of kidney function over time. Many patients remain asymptomatic until the advanced stages, so diagnosis often comes too late for therapeutic intervention. Fibrosis is the pathophysiological hallmark of progressive CKD regardless of the initial etiology of injury and, if unchecked, may eventually overwhelm the functional tissue leading to end-stage kidney disease (Zeisberg and Neilson, 2010). Morphologically, fibrosis is characterized by increased numbers of activated fibroblasts, excessive accumulation of extracellular matrix, vascular rarefaction and tubular atrophy as a result of a shift in these cells from an epithelial to mesenchymal phenotype, and insufficient regeneration. It often coexists with, or is preceded by, inflammation and is triggered by severe or recurrent acute injury (Basile et al., 2016). Accumulating evidence suggests that acutely damaged proximal tubular epithelial cells (PTECs) drive the fibrotic process through the release of pro-inflammatory and pro-fibrotic cytokines. Key signaling pathways have been identified including many that are important in embryonic development, cancer progression, and inflammation (Bonventre, 2014; Guzzi et al., 2019).

[1]Renal Sciences, Department of Inflammation Biology, School of Immunology & Microbial Sciences, Faculty of Life Sciences and Medicine, King's College London, SE5 9NU London, UK

[2]School of Life Sciences, Gwangju Institute of Science and Technology, Gwangju, Republic of Korea, 61005

[3]Centre for Host–Microbiome Interactions, Faculty of Dentistry, Oral & Craniofacial Sciences, King's College London, SE1 9RT London, UK

[4]Science for Life Laboratory (SciLifeLab), KTH - Royal Institute of Technology, Tomtebodavägen 23, Solna, Stockholm 171 65, Sweden

[5]Lead contact

*Correspondence: adilm@scilifelab.se (A.M.), saeed.shoaie@kcl.ac.uk (S.S.), claire.sharpe@kcl.ac.uk (C.C.S.)

https://doi.org/10.1016/j.isci.2021.102046

More recently, both acute kidney injury (AKI) and CKD have been demonstrated to be associated with significant shifts in renal cell metabolism, again most importantly, in the PTECs (Balzer and Susztak, 2020; Chen et al., 2017; Kang et al., 2015). It has been postulated that this metabolic dysfunction is directly causative in the pathogenesis of renal fibrosis based on the intracellular deposition of triglycerides and a decrease in fatty acid oxidation (FAO) in a folic acid-induced mouse model of renal fibrosis. This was associated with lower transcriptional levels of peroxisome proliferator-activated receptor alpha (PPAR-alpha) and peroxisome proliferator-activated receptor gamma coactivator 1-alpha (PPARGC-1a), enzymes involved in lipid and energy metabolism (Kang et al., 2015). However, this model was interrogated in a relatively acute phase (7 days post folic acid injection) and was not able to assess changes over time. The same study also showed that TGF-β1 induction in renal epithelial cells suppresses FAO in a PPARGC-1a-dependent manner.

In addition, Lu et al. have shown that PPAR-γ stimulation prevents fibroblast proliferation through the induction of platelet-derived growth factor (PDGF) and phosphorylation of AKT (Lu et al., 2016), whereas others have shown that abnormal mitochondrial activity and impaired glycolysis and FAO are important features of polycystic kidney disease (Padovano et al., 2018; Podrini et al., 2018; Rowe et al., 2013). Moreover, mitochondrial transcription factor A (TFAM) plays a key role in the regulation of mitochondrial DNA transcription and the expression of its gene TFAM is negatively correlated with the degree of renal fibrosis in the kidneys of patients with CKD (Chung et al., 2019; Scarpulla, 2008). In this study, transgenic mice missing the TFAM gene in renal tubular cells alone developed metabolic dysfunction, mitochondrial loss, renal fibrosis, and immune cell infiltration by 6 weeks of age, suggesting a causal relationship between metabolic dysfunction in tubular cells and inflammation and fibrosis in the kidney.

The interplay between inflammation, fibrosis, and metabolism in the progression of CKD is thus complex and difficult to tease apart. Unbiased, systems biology-based approaches and multiomics analysis can be usefully employed to interrogate these interactions, to discover biomarkers and to identify drug targets. To date, the valuable systems biology tools, genome-scale metabolic models (GEMs), have been generated for different tissues and used in the integration of multiomics data to gain understanding of metabolism-related disorders including obesity, fatty liver disease, diabetes, and certain types of cancers (Mardinoglu et al., 2018; Mardinoglu and Nielsen, 2015; O'Brien et al., 2015). Here, we have used an omics approach and integrative computational modeling to investigate the relationship between inflammation, fibrosis, and changes in metabolism over time in a longitudinal mouse model of fibrosis and CKD following aristolochic acid (AA)-induced AKI.

RESULTS

Intraperitoneal injection of aristolochic acid induces acute kidney injury, which leads to progressive chronic kidney disease in mice

Aristolochic acid nephropathy (AAN) is an important and probably under-reported global cause of CKD and has been used to model AKI and CKD in rodents for over 30 years (Jadot et al., 2017; Ortiz et al., 2015). In this study, we adapted a murine model of aristolochic acid (AA)-induced AKI, which is associated with low mortality but progresses to fibrotic CKD leading to established renal impairment over 100 days. We used outbred CD1 mice, which are susceptible to developing renal fibrosis (Walkin et al., 2013), and injected them with two low doses of AA (3.5 mg/kg) by intraperitoneal injection on day 0 and day 5 (Figure 1A, see Transparent methods). By measuring the serum blood urea nitrogen and creatinine on day 12, the significant and early rapid rise confirmed the presence of AKI, which recovered (with respect to renal function) by day 32, although not completely back to baseline (early CKD) (Figures 1B and 1C). This was followed by a slow second decline in renal function to day 100 (late CKD) confirming the disease progression without further intervention. Histological analysis using picrosirius red staining and biochemical analysis of hydroxyproline content of the tissue confirmed the presence of increased collagen deposition in the tissue over time in keeping with progressive fibrosis (Figure 1D).

Differentially expressed genes are clustered by treatment rather than time point of the model

Next, to better understand the longitudinal changes and molecular mechanism underlying the progression of CKD following AKI, we performed transcriptome analysis by RNA-sequencing, generating an average of 8.8 million reads per sample on mouse kidney tissues during both early (day 32) and late (day 100) stages of CKD, together with age-matched controls with triplicates for each group.

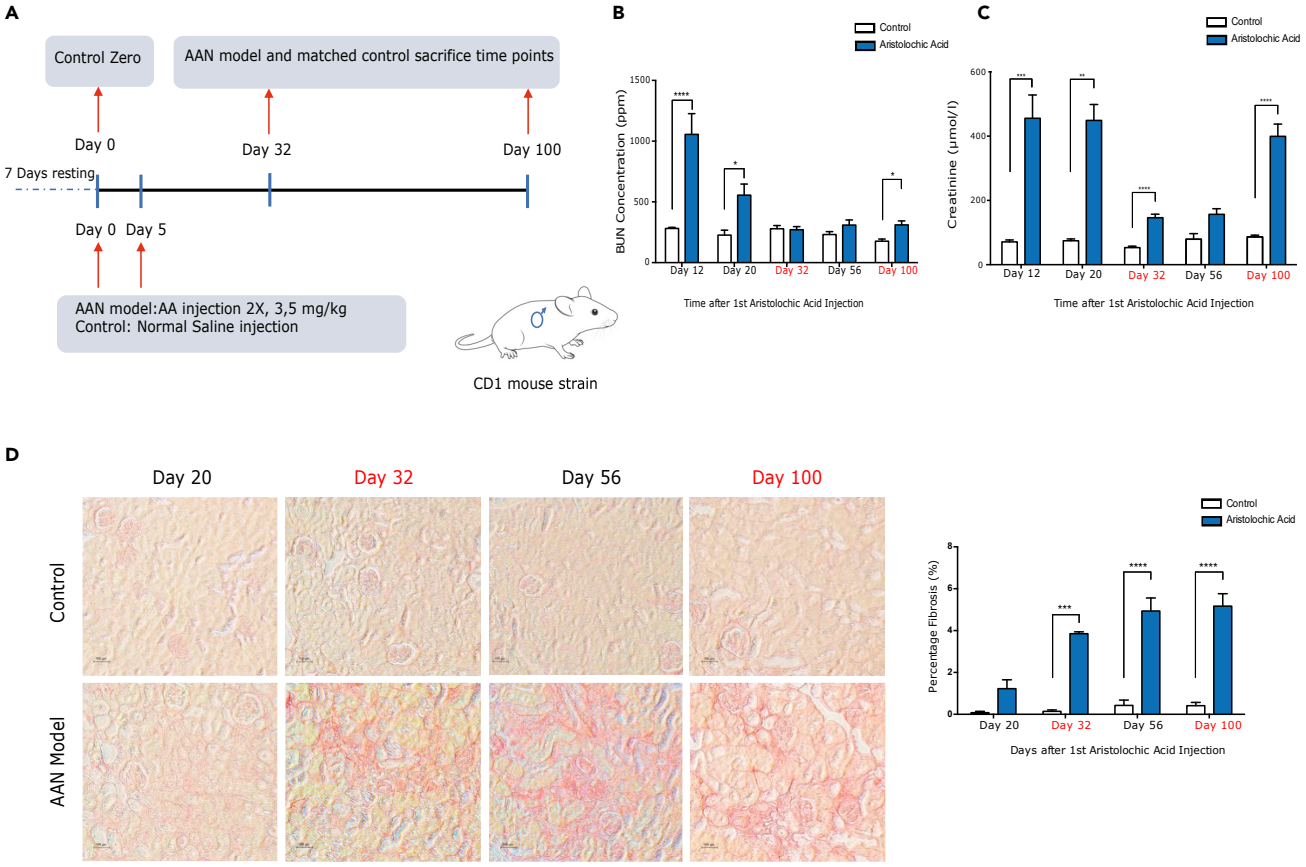

Figure 1. Intraperitoneal injection of aristolochic acid induces acute kidney injury, which leads to progressive chronic kidney disease in mice

(A) Two 3.5-mg/kg aristolochic acid injections (or normal saline vehicle) were given 5 days apart to 8-week-old CD1 mice. After 32 and 100 days, mice were sacrificed with their saline-injected age-matched controls (N = 3 per group).

(B) Serum blood urea nitrogen (BUN) levels at different time points; p value < 0.0001 at Day 12, p value = 0.0394 at Day 20, p value = 0.0194 at Day 100.

(C) Serum creatinine levels at different time points; p value < 0.0007 at Day 12, p value = 0.0013 at Day 20, p value < 0.0001 at Day 30, p value < 0.0001 at Day 100.

(D) Picro Sirius red staining of kidney tissue for collagen deposition and area fraction quantification. Scale bars = 100µm

By performing principal component analysis (PCA) on transcriptomes of all samples (Figure 2A), we observed significant clustering by treatment with AA (permutational multivariate analysis of variance (PERMANOVA) p value < 0.001), rather than time points (PERMANOVA p value = 0.107). To determine the gene expression changes by the AA treatment, we identified significantly differentially expressed genes (DEGs) at different time points and conditions using the DESeq package (Anders and Huber, 2010). We found that 2,124 unique genes were upregulated and 1,403 unique genes were downregulated at day 32, and 399 were upregulated and 437 were downregulated at day 100, comparing AA-treated samples with age-matched controls (negative binomial tests, adjusted p value < 0.05; Table S1). Among these DEGs, 611 were commonly shared at both days 32 and 100, with 286 upregulated at day 32 and day 100 and 325 downregulated at both time points (Figure 2B). Of interest, seven DEGs had opposite expression directionality between day 32 and day 100 (Figure 2C). These included *Eng* (encoding endoglin) and *Plvap*, which were upregulated at day 32 but downregulated at day 100. DEGs that were upregulated at day 32 but not differentially expressed at day 100 included *Flt1*, *Kdr*, and *Flt4*, which encode for fms-like tyrosine kinase1 or vascular endothelial growth factor receptor 1 (VEGFR1), fetal liver kinase-1 or vascular endothelial growth factor receptor 2 (VEGFR2), and fms-like tyrosine kinase 4 or vascular endothelial growth factor receptor 3 (VEGFR3).

Collagen turnover and inflammation pathways were upregulated in both early and late CKD

Next, we performed gene enrichment analysis using Database for Annotation, Visualization and Integrated Discovery (DAVID) to identify biological processes significantly enriched with DEGs (Fresno and Fernandez,

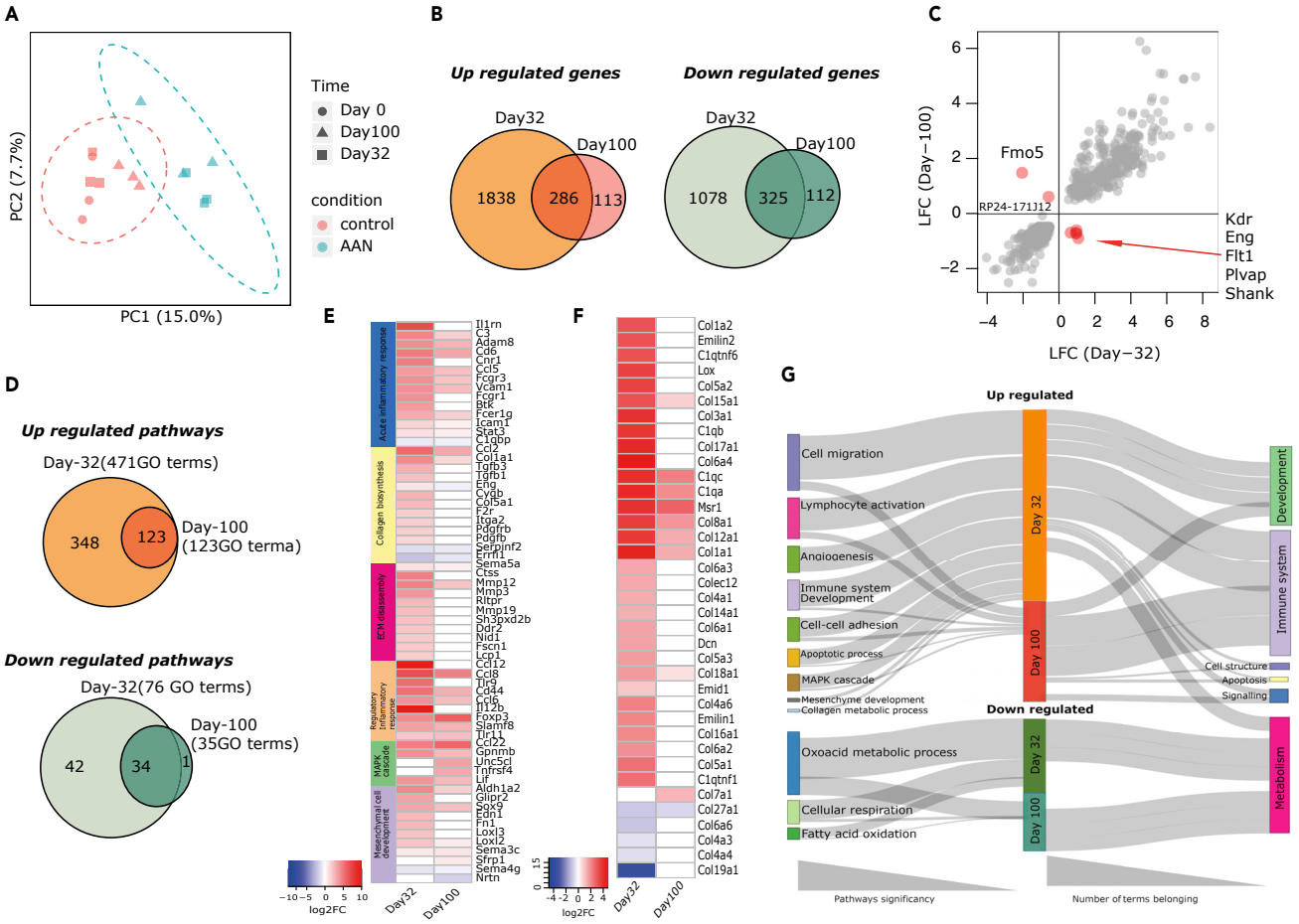

Figure 2. Differentially expressed genes are clustered by treatment rather than time point of the model

(A) Principal component analysis of global transcriptomic data derived from kidney tissue of AAN murine model and age-matched controls at different time points.

(B) Venn diagram showing shared significantly up/downregulated genes at day 32 and day 100 in AAN compared with age-matched controls.

(C) Scatterplot showing fold changes of differentially expressed genes (DEGs) comparing day 32 and day 100. Dots in red are genes that show opposite direction of expression between the two time points.

(D) Venn diagram shows enriched pathways of up/downregulated DEG (FDR <0.05).

(E) Heatmap showing the six most significantly enriched pathways involved in inflammation and fibrosis and the most highly upregulated genes (top 10) of each pathway at day 32 and day 100 (log_2 fold change).

(F) Heatmap showing the differential expression of genes involved in collagen production at day 32 and day 100 (log_2 fold change).

(G) Sankey diagram of enriched pathways of up/downregulated genes. Here we present detailed classes of enriched pathways in the left-hand nodes and broad definitions in the right-hand nodes. The thickness of the gray connectors coming from the left side depicts the significance of the given class of enriched pathway at each time point. The thickness of the gray connectors coming from the right side depicts the number of enriched terms belonging to the given pathway at each time point.

2013; Huang da et al., 2009). Here, we observed significant overlap of enriched biological process terms between day 32 and day 100 (false discovery rate [FDR] <0.05; Figure 2D, Table S2). Using the MGI-MGD database (Smith et al., 2018), we investigated the significant DEGs within the five key pathways involved in fibrosis and determined the changes in genes involved in collagen expression and degradation to study collagen turnover during early and late stages of CKD (Figures 2E and 2F). We found that the majority of genes involved in collagen expression and degradation were significantly upregulated at day 32 and also at day 100, although to a lesser degree, in keeping with a progressively fibrotic model (negative binomial tests, adjusted p value <0.05). Next, despite almost complete resolution of kidney function by day 32, we observed that inflammation pathways were also highly upregulated in this early CKD stage and remained upregulated, although to a lesser extent at day 100, in a similar pattern to the fibrosis pathways (Figure 2G).

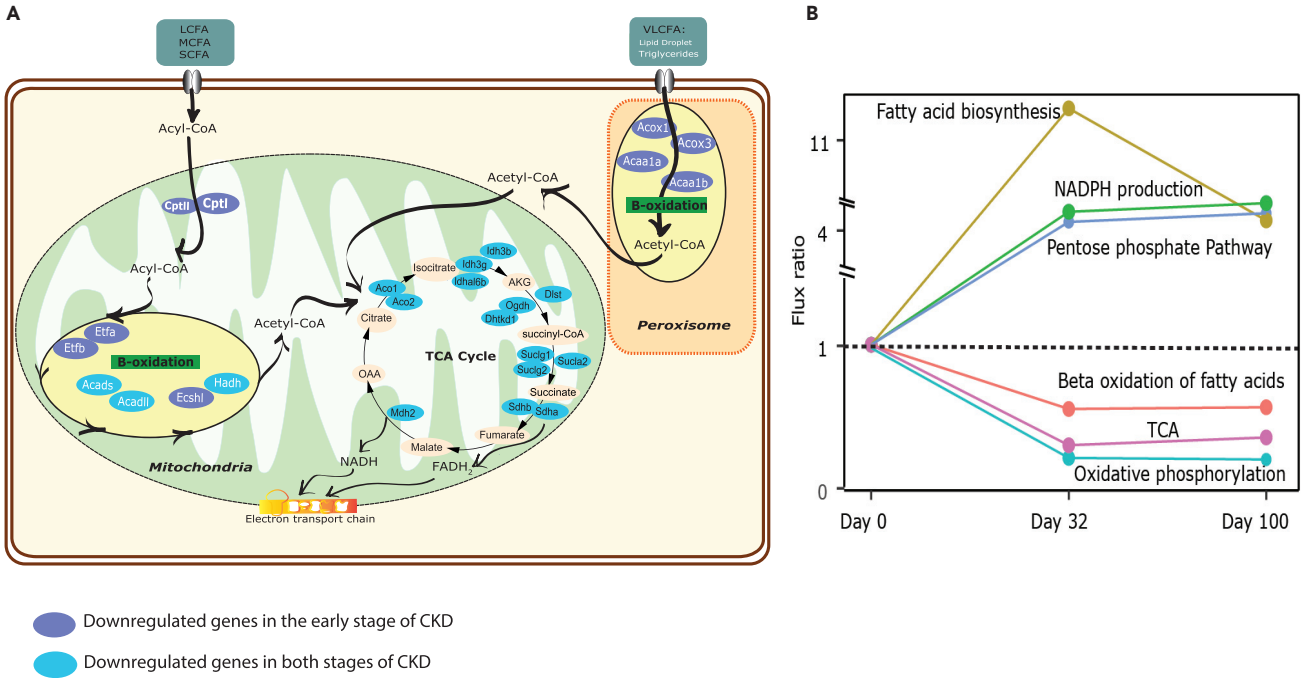

Figure 3. Peroxisomal and mitochondrial fatty acid oxidation are dysregulated in both early and late CKD

(A) Diagram depicting dysregulation of fatty acid oxidation in both peroxisomes and mitochondria. Genes in purple are those downregulated in early CKD (day 32) in the β-oxidation pathway in both peroxisome and mitochondria. Genes in blue are those downregulated at both stages of CKD in the TCA cycle and β-oxidation pathways in mitochondria.

(B) Diagram showing the average predicted flux ratio for the metabolic pathways on days 32 and 100 compared with control (baseline); positive and negative flux ratios indicate increased and decreased flux at both stages of CKD, respectively.

In contrast to the upregulation of inflammation and collagen turnover pathways, gene ontology pathway analysis of metabolism-associated genes showed downregulation of energy metabolism, fatty acid oxidation, and oxoacid metabolic processes, which consist of aerobic respiration, ATP synthesis-coupled electron transport, glutathione metabolism, cell redox homeostasis, and glycolytic processes (Figure 2G). Similarly to inflammation and fibrosis, these changes were greatest at day 32, although they did persist at day 100 resulting in a negative correlation of gene expression related to inflammation and fatty acid metabolism (Figure S1).

Peroxisomal and mitochondrial fatty acid oxidation are dysregulated in both early and late CKD

Based on the biological process and DEGs from previous sections, we observed dysregulation in the glycolysis, tricarboxylic acid (TCA) cycle, and oxidative phosphorylation (OXPHOS) and oxidative stress pathways (Figure 3A). Most of the genes involved in glycolysis and the TCA cycle and several genes involved in the regulation of reactive oxygen species were noticeably downregulated (negative binomial tests adjusted p values < 0.05; Table S3). Of interest, the observed pattern of DEGs suggested that there was a significant decrease in the activity of proliferator-activated receptors (PPARs), which control the expression of genes involved in fatty acid β-oxidation via the peroxisome pathway and mitochondria of the AAN mice. In the early-stage CKD model, *Cpt1α* and *Cpt2* (carnitine palmitoyl transferase I and II), which facilitate the transportation of fatty acid into mitochondria for energy production, were downregulated. In both early- and late-stage CKD models, we observed a downregulation of genes involved in mitochondrial β-oxidation of fatty acids, such as *Acads* (encoding acyl-CoA dehydrogenase short chain), *Acad11* (encoding acyl-coenzyme A dehydrogenase family enzyme 11), *Hadh* (encoding hydroxyacyl-CoA dehydrogenase), and *Mlycd* (encoding malonyl-CoA decarboxylase), which converts malonyl-CoA to acetyl-CoA in both the mitochondria and the peroxisome.

In the peroxisome, *Tysnd1* (encoding peroxisomal leader peptide-processing protease) was also downregulated in both early and late stages and encodes crucial enzymes for fatty acid shortening and fatty acid

oxidation (Chegary et al., 2009; Mizuno et al., 2013). *Acox1* and *Acox3*, which encode the proteins peroxisomal acyl-coenzyme A oxidase 1 and 3, respectively, were downregulated only in early CKD and catalyze the desaturation of acyl-CoAs to 2-trans-enoyl-CoAs in peroxisomal fatty acid β-oxidation, a reaction that donates electrons directly to oxygen molecule thereby producing hydrogen peroxide (Varanasi et al., 1994). Defects in these genes lead to accumulation of very-long-chain fatty acids. *Acaa1* was also downregulated in early CKD and encodes the enzyme acetyl-CoA C-acyltransferase involved in fatty acid β-oxidation and degradation. The *Phyh* gene was highly downregulated in both early and late stages of our CKD model and encodes for phytanoyl-CoA hydroxylase. This enzyme breaks down the plant-derived fatty acid phytanic acid in the peroxisome via an α-oxidation process, the products of which are then further broken down via β-oxidation (Jansen et al., 2000).

Transcriptome data from both stages of CKD showed significant reduction in the mitochondrial estrogen-related receptor alpha (*Esrra*) gene. This transcription factor is involved in mitochondrial biogenesis and is downregulated in both early and late CKD, but more significantly so in late CKD (Bookout et al., 2006). We also observed a decrease in the expression of other important mitochondrial genes that encode subunit enzymes that participate in mitochondrial oxidative phosphorylation, such as cytochrome *c* oxidase 5a/b and 6 (*Cox 5a/b* and *Cox 6*) (Reinecke et al., 2009). Conversely, there were no downregulated genes at day 100 involved in peroxisome fatty acid β-oxidation. *Crot* (encoding peroxisomal carnitine O-octanoyltransferase), which catalyzes the reversible transfer of fatty acyl groups between CoA and carnitine, facilitating the transport of medium-length acyl chains out of the mammalian peroxisome to the cytosol and mitochondria for degradation, was upregulated.

Of interest, in early CKD in our model, many genes that are involved in inositol phosphate metabolism and production of myo-inositol (MI) were highly upregulated, such as *Inpp5d* (encoding inositol polyphosphate-5-phosphatase D), *Pip4k2a/b* (encoding phosphatidylinositol-5-phosphate 4-kinase type II alpha and beta), and *PTEN* genes, whereas the gene for myo-inositol oxygenase (MIOX), an enzyme responsible for catalyzing the degradation of MI into D-glucuronic acid, was significantly downregulated. Moreover, despite downregulation of the glycolysis pathway, the gene for hexokinase 3 (HK3), a key enzyme in the first step of glucose metabolism, which produces glucose-6-phosphate (G6P), was significantly upregulated. Therefore, it would seem likely that this G6P further increases the biosynthesis of MI as it is a substrate for inositol-3-phosphate synthase, the gene for which (*ISYNA1)* was also significantly upregulated in our model.

Flux balance analysis suggests a drop in overall flux in both mitochondria and peroxisome

To better understand the impact of early and late CKD gene expression changes on renal cell metabolism, we used GEM of the kidney tissue based on the transcriptomic data. The applied GEM consisted of 3,579 genes, 8,140 reactions, and 5,516 unique metabolites at 8 different cellular compartments (Mardinoglu et al., 2015). Initially, we integrated the transcriptional data of the three time points (baseline, day 32, and day 100) on the kidney GEM. To further elucidate the metabolic flux within the cell, we performed constraint-based modeling using the transcriptional data as the main constraint (see Transparent methods). Three specific constrained models were generated based on the transcriptional data from baseline, early CKD (day 32), and late CKD (day 100). To perform flux balance analysis (FBA) and predict the flux distribution in each time point, the maximization of ATP demand reaction was considered as the desired cellular objective (Orth et al., 2010). The outputs of the simulations confirmed that the metabolic flux through the aforementioned pathways was reduced in early CKD versus control (baseline); however, there was a slight increase in the overall flux for late versus early CKD (Figure 3B, Table S4). The simulations also predicted a major increase through the pentose phosphate pathway, NADPH production, and fatty acid biosynthesis supporting the observation that there is reprogramming of the metabolic flux from glycolysis to the pentose phosphate pathway through glucose-6-phosphate. This is likely to lead to an increase in the production of NADPH, fatty acid biosynthesis, and an increase of inositol phosphate metabolism, as we observed from our gene expression data. GEM simulations also showed that the overall flux in both mitochondrial and peroxisomal β-oxidation is decreased, as is the flux through oxidative phosphorylation, confirming the reduction of mitochondrial activity. In healthy renal tissue (baseline) the acetyl-CoA turnover rate is high, being predominantly produced by fatty acid β-oxidation and glycolysis and consumed by the TCA pathway. Conversely, in CKD, especially at the early stage, acetyl-CoA is converted to malonyl-CoA for fatty acid biosynthesis. Of interest, the acetyl-CoA is mainly provided by the catabolism of branched-chain amino acids, especially isoleucine (Table S4).

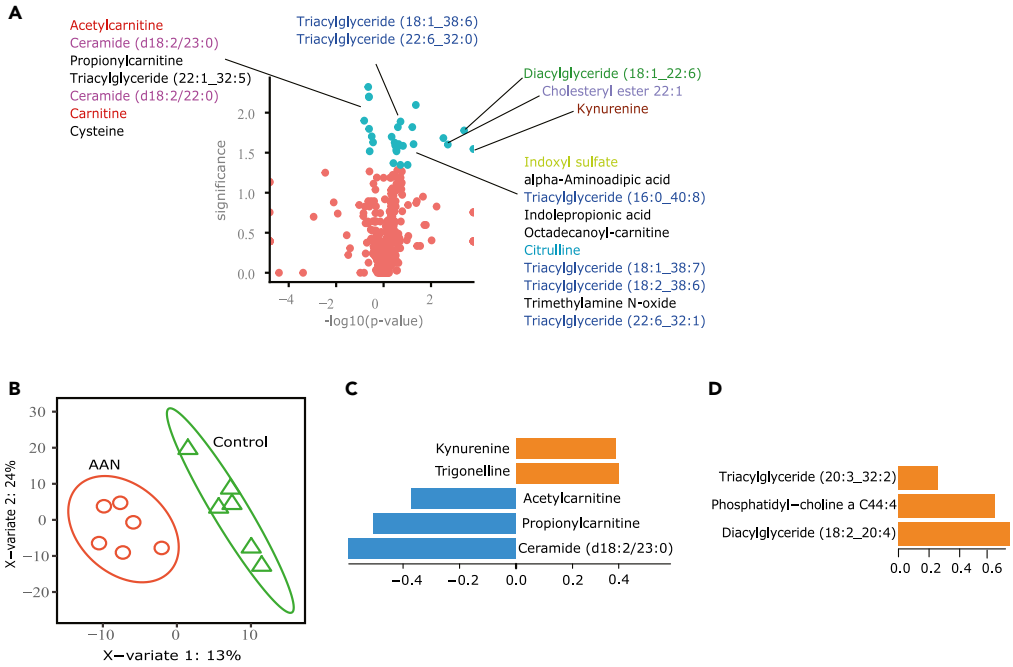

Figure 4. Serum metabolic profiles in mice with AA nephropathy demonstrate an increase in circulating LCFA

(A) Scatterplot showing how the concentrations of different metabolites vary according to disease versus age-matched controls (day 32 and day 100 data combined). Blue dots represent metabolites with significantly changed concentrations (p value < 0.05) and red dots show those without significant changes (Wilcoxon test, p value<0.05, $\log_2$ fold change).

(B) Partial least squares-discriminant analysis (PLS-DA) comparison of metabolite concentration levels in different serum samples (disease versus no disease).

(C) Changes in metabolites that are common for both early and late CKD compared with age-matched controls.

(D) Changes in metabolites that are specific for early CKD compared with age-matched controls.

Consistent with FBA, the reporter metabolite analysis showed that NAD+, NADH, ubiquinol, ubiquinone, CoA, FAD H2 (reduced flavin adenine dinucleotide), acetyl-CoA, glycerate, glutamine-alpha-ketoglutarate (AKG), and pyruvate are the main significantly decreased reporter metabolites (whereby the expression of the genes in relation to the metabolites is decreased) from baseline to day 32 (Figure S2, Table S5), in keeping with our data suggesting mitochondrial dysfunction in early CKD. Of interest, the reporter metabolites ubiquinone, ubiquinol, NADH, NAD+, ferricytochrome C, and ferrocytochrome C were significantly upregulated in late CKD (day 100) in comparison with early CKD (day 32), which might suggest some improvement of mitochondrial function over time. Our previous pathway and DEGs analysis, together with modeling, demonstrates the decrease of fatty acid oxidation in both early and late stages of CKD, whereas the modeling shows an increase of fatty acids biosynthesis in early CKD. In addition, we observed the upregulation of genes responsible for choline and lysosomal proteolysis, which would include degradation of albumin and extracellular matrix proteins in early CKD compared with healthy tissue.

Serum metabolic profile in mice with AA nephropathy demonstrates an increase in circulating LCFA

To test our prediction that CKD induced by AAN leads to increased long chain fatty acid (LCFA) metabolites, we performed targeted metabolomics on the sera from the same mice we used for the transcriptomic analysis. Initially, we compared all diseased (both early and late CKD combined) with age-matched controls by performing the Wilcoxon signed-rank test (p value < 0.05; Figure 4A, Table S6). The majority of metabolites that were found to be increased in the serum were triglycerides (an ester derived from glycerol and three long-chain fatty acid molecules). Also, among the top significantly changed metabolites were diacylglyceride (DAG), another high-density lipid, and cholesteryl ester demonstrating raised lipoproteins in the serum. Kynurenine and indoxyl sulfate, so-called uremic toxins, were also increased in AAN. These two metabolites are the product of tryptophan degradation and are known to be elevated in patients with CKD (Tan et al., 2017). Of interest, the serum level of carnitine and two other carnitine-related

metabolites, acetyl carnitine and propionyl carnitine, were decreased in the serum of AA nephropathy mice compared with controls, in keeping with previous reports of reduced circulating levels of carnitine in patients with CKD (Calvani et al., 2004; Charnas et al., 1991). Similarly, reduced ceramide has previously been associated with advanced CKD (Reis et al., 2015). In addition, another two metabolites, Kynurenine and Citrulline, were increased in our serum samples. These two metabolites previously were indicated as a CKD development marker in patients' plasma (Rhee et al., 2013).

In order to further distinguish between the metabolites in the serum of AAN mice and their age-matched controls, partial least squares discriminant analysis (PLS-DA) was applied (Figure 4B). The output of this analysis was highly consistent with the results from the Wilcoxon signed-rank test, showing significant changes in the same metabolites, comparing AAN and controls. As seen in Figure 4C, an elevation in kynurenine and reduction in circulating acetylcarnitine and propionyl carnitine were among the indicators of early and late stages of CKD in AAN compared with controls, whereas a rise in tri(di)acylglyceride and phosphatidylcholine metabolites was the signature of early CKD in AAN (Figure 4D).

Global transcriptomics in proximal tubular cells undergoing transition from epithelial to mesenchymal phenotype *in vitro* shows similar FAO dysregulation

To further investigate the relative impact of AAN on different cell types within the kidney, we checked differential gene expressions by the cell type maker genes of kidney tissues (i.e., $\log_2$ fold changes, Figure S3), which were previously identified from single cell transcriptomics data (Park et al., 2018). Of interest, we found considerable downregulation of expression of proximal tubule cell markers at day 32 and substantial upregulation of expression of cell markers of macrophages, T lymphocytes, neutrophils, and fibroblasts, in keeping with a state of ongoing inflammation and fibrosis. At day 100, we observed again a significant downregulation of proximal tubule cell markers and an upregulation of expression of cell markers of inflammation and fibrosis. Of interest, endothelial cell markers were significantly upregulated on day 32 but downregulated by day 100. We also interrogated enriched biological process terms of cell markers of each cell type confirming that the proximal tubule cell is responsible for fatty acid oxidation within the kidney, in keeping with our metabolomic data (Table S7).

PTECs are the most metabolically active cells in the kidney, so we hypothesized that changes in the metabolism within these cells are the main drivers for the results described above. To test this, we developed an *in vitro* CD1 mouse proximal tubular epithelial cell (MPTEC) model, which could mimic changes associated with epithelial-mesenchymal transition (EMT). PTECs are thought to partially undergo this process during fibrogenesis, and this model is a well-established *in vitro* model of fibrosis (Lovisa et al., 2016). We quantified cell line transcriptomes with average 8.4 million mapped reads from MPTEC cell lines, which were treated with two cytokines, TGF-β and EGF (10 ng/mL each) versus untreated cells. Cell analysis was undertaken at three time points, along with matched controls, following 1, 3, and 5 days of treatment (Figures 5A and 5B, see Transparent methods). Morphological transformation from epithelial to mesenchymal phenotype triggered by these cytokines was noted at day 3 and day 5 with reduced expression of the epithelial cell marker E-cadherin, an increase in α-smooth muscle actin (α-SMA) expression, and formation of mesenchymal-like F-actin stress fibers seen by phalloidin staining (Figure 5C).

By performing PCA on the *in vitro* model transcriptomes, we found that samples were significantly clustered by both treatment conditions (PERMANOVA p value < 0.001) and time points (PERMANOVA p value < 0.002), particularly in those cells treated for 5 days (Figure 6A). Based on negative binomial tests of the DESeq package (Anders and Huber, 2010), we identified an average of 1,539 DEGs per each time point including a subset of genes, which were significantly differentially expressed at all time points (Figure S4A, adjusted p value $< 1 \times 10^{-5}$); 150 upregulated genes and 127 genes downregulated (Figure S4B, Table S8). Among the DEGs observed at all three time points, we found that fold changes were similar at all time points.

When we compared enriched biological process terms using DAVID (FDR <0.05) (Fresno and Fernandez, 2013; Huang da et al., 2009), we found overlap of several upregulated pathways at different time points but less overlap for downregulated pathways (Figure S4C, Table S9). Fifty-two biological process terms were enriched among upregulated genes at all time points, but none of them were commonly enriched among downregulated genes, implying time-specific repressions. Cell migration (contained within the larger term of development) and apoptosis were common at all three time points in upregulated enriched

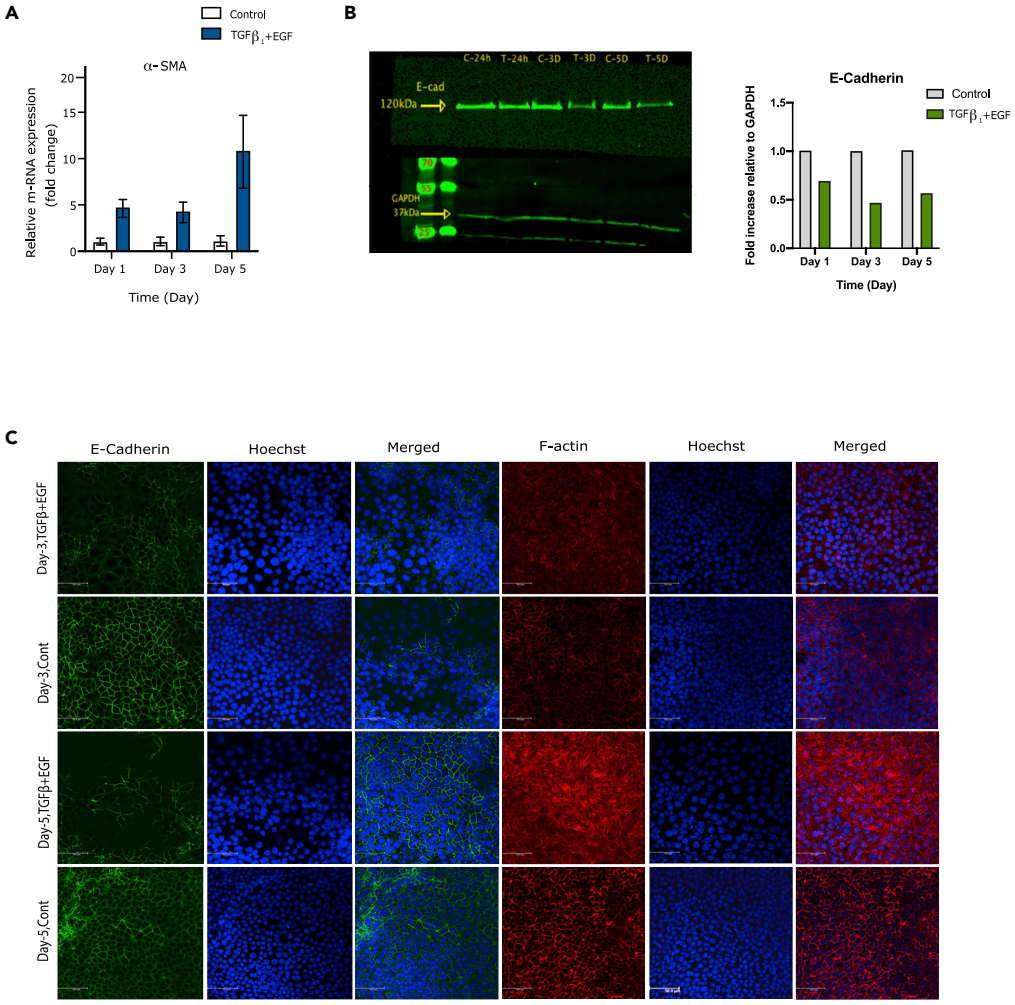

Figure 5. Proximal tubular cells undergo epithelial to mesenchymal transition *in vitro* when treated with TGF-β1 and EGF

MPTECs were treated with 10 ng/μL each of TGF-β1 and EGF to induce epithelial to mesenchymal transition.

(A) Quantitative determination of α-SMA mRNA expression at different time points of treatment compared with untreated controls. α-SMA expression was measured using q-PCR (number of replications = 3, house-keeping gene: GAPDH). Two-way ANOVA test, p value = 0.02. Data are represented as mean ± SD.

(B) E-cadherin expression determined by densitometry of western blot at different time points compared with untreated controls.

(C) Immunofluorescence staining for E-cadherin with anti-E-cadherin and Alexa Flour 488 (green), and F-actin localization using Rhodamine phalloidin (red) after 3 and 5 days of treatment. Nuclei are stained using with Hoechst (blue) (40× magnification and scale bar, 50μm).

pathways, and mitochondrial metabolic pathways were among the downregulated enriched pathways following 5 days of treatment (Figure 6B). Of interest, pathways known to be downstream of TGF-β were enriched at day 1 and day 3 (but not at day 5) as were mesenchymal pathways, in keeping with a process of EMT.

As hypothesized, tubular metabolic pathway responses to treatment with the two cytokines at day 5 were consistent with our *in vivo* model of CKD. We saw significant downregulation of genes involved in glycolysis, and the TCA cycle showed major disruption in central carbon metabolism pathways. To further examine alterations in FAO pathways in mitochondria and peroxisomes in our *in vitro* model, we looked at changes in the genes involved in fatty acid degradation, fatty acid β-oxidation, and peroxisome proliferator-activated receptors (PPARs)-induced pathways. Transcriptional change in downstream genes of the PPAR transcription factor,

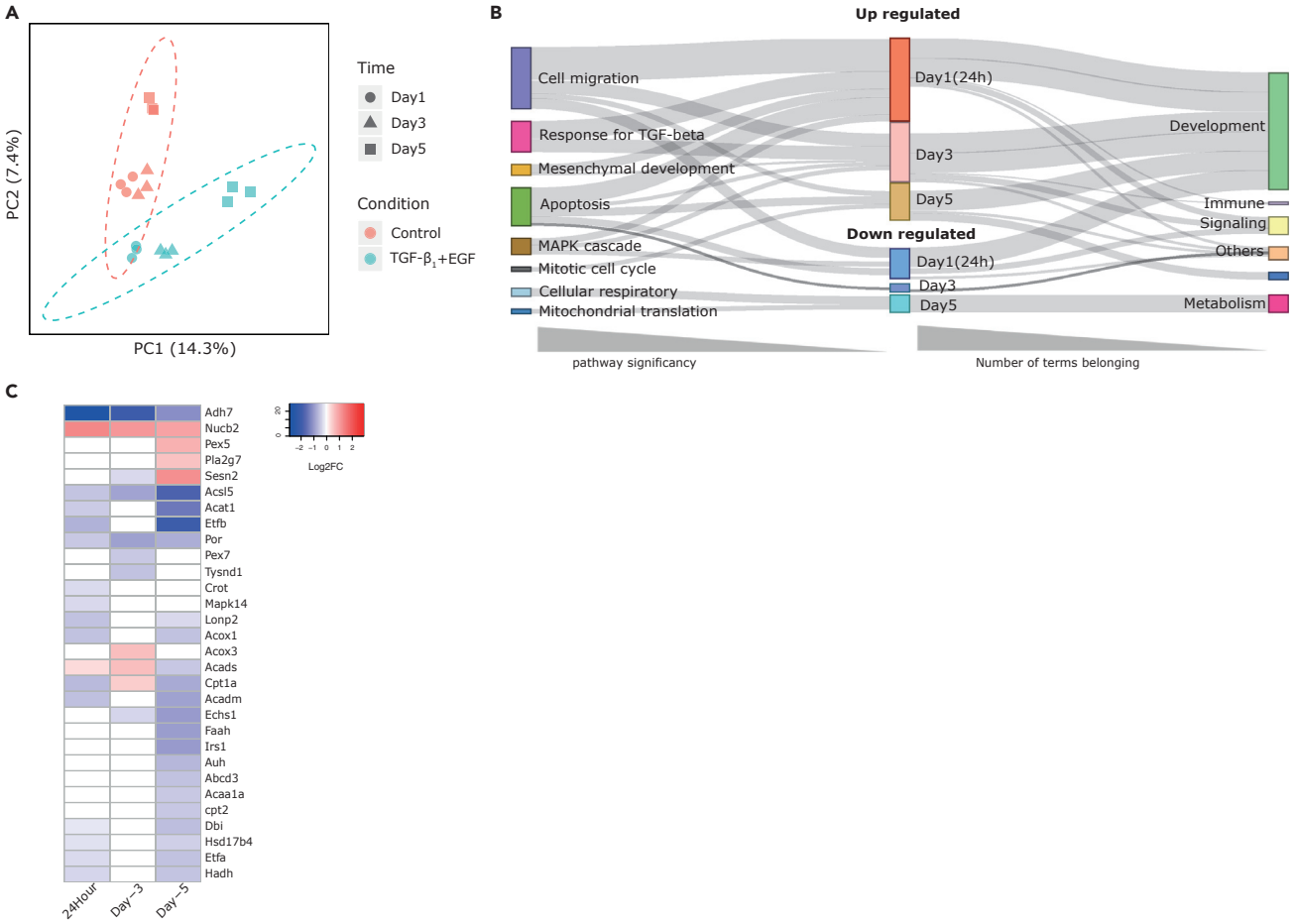

Figure 6. Global transcriptomics in proximal tubular cells undergoing transition from epithelial to mesenchymal phenotype *in vitro* shows similar FAO dysregulation

(A) Principal component analysis of global transcriptomic data derived from the *in vitro* model of EMT at different time points demonstrating clustering by treatment rather than time point.

(B) Sankey diagram of enriched pathway of up/downregulated genes in mouse proximal epithelial cells at days 1, 3, and 5. The graph illustrates the enriched biological processes (left nodes) among upregulated or downregulated DEGs at different time points in the middle (24 h, day 3, and day 5). The general terms for significantly changed pathways are shown in the nodes on the right side.

(C) Heatmap showing upregulated (red)/downregulated (blue) genes in peroxisome and mitochondrial FAO pathways during EMT (see also Figure S4).

such as *Cpt1a* and *Cpt2*, *Acads*, *Hadh*, and *Etfa*, suggested that the most downregulated genes were those that encode vital enzymes in fatty acid shortening and fatty acid oxidation (Figure 6C). In addition, genes encoding enzymes involved in peroxisome β-oxidation/degradation, such as *Acox1* and *Acaa1*, were downregulated at day 5, in a similar way to the AAN tissue, and *Por* (Cytochrome P450 oxidoreductase), which plays a role in fatty acid and steroid metabolism, was among the genes that were downregulated at all three time points in our *in vitro* model and both early and late CKD in the AAN model.

DISCUSSION

In this study we aimed to define changes in molecular mechanisms and metabolic pathways at different stages of CKD following AKI using genome-wide transcriptomics, metabolomics, and computational modeling in a mouse model of aristolochic acid-induced nephropathy. In addition, we further investigated the impact of fibrotic stimuli on an *in vitro* model of epithelial to mesenchymal transition of MPTECs to more specifically interrogate the changes occurring in this key cell type.

In the early stages of CKD, immediately following recovery from AKI, our transcriptomic data demonstrated a marked upregulation of the inflammatory response mirrored by similar changes in pro-fibrotic pathways

and matrix assembly and disassembly. In conjunction with this, there were marked reductions in the genes responsible for fatty acid oxidation, the tricarboxylic acid cycle, and oxidative phosphorylation. Of interest, these derangements in metabolic genes persisted for the full length of the model, through to the late stages of CKD, whereas the upregulation of genes involved in the inflammatory component subsided with time, as did the upregulation of genes involved in matrix turnover. Endothelial cell markers were significantly upregulated in early CKD but downregulated by day 100. Endothelial cell proliferation is known to occur in the immediate post-AKI period in response to an increase in the release of angiogenic factors, particularly from PTECs (Ohashi et al., 2002). However, as CKD develops, release of these factors declines and epithelial cells undergo apoptosis. Alongside this, the pericytes that normally maintain vascular integrity migrate into the renal interstitium and become myofibroblasts, contributing to the progression of the fibrotic process. Migration of pericytes away from the vasculature results in vascular rarefaction, which is a hallmark of progressive CKD (Kida, 2020).

PTECs are highly enriched with mitochondria and depend largely on FAO and oxidative phosphorylation to fulfill their high-energy requirements, and we are not alone in demonstrating that renal cell metabolism (predominantly PTECs) is dysregulated in both AKI and CKD, with downregulation of FAO (Li et al., 2017; Marx et al., 2018) (Kang et al., 2015). Until recently, it has been thought that injury leads to inflammation, which in turn leads to metabolic dysfunction, progressive fibrosis, and CKD (Anders and Schaefer, 2014; Basile et al., 2016). However, Chung et al. have clearly demonstrated that compromised mitochondrial integrity (as a result of acute injury) leads to leakage of mitochondrial DNA from cells, which in turn triggers an inflammatory response via activation of STING (Chung et al., 2019). This paradigm shift therefore suggests that persistent inflammation may come secondary to the acute changes in metabolism that we and others have observed. One important difference between our study and the preceding ones is the longitudinal nature of our model. The persistence of the metabolic derangement at 100 days, despite a fall in inflammation, may suggest that the reduction in normal mitochondrial activity does not fully recover, even when the acute injury has resolved. This would be in keeping with a greater burden of fibrosis and the tubular atrophy that we know is the hallmark of CKD, which may be driven by a continuing increase in oxidative stress. Alongside this, we have shown that metabolism is shifted from FAO and glycolysis to the pentose phosphate pathway, which occurs exclusively in the cytosol.

We have also undertaken the computational flux balance modeling, together with analyzing transcriptomic data and targeted metabolomics of the mouse sera. This has revealed that, over time, serum levels of triglycerides and diacylglyceride accumulate in the serum of mice with CKD. Dyslipidemia has been known to be associated with CKD for many years. The pattern is similar to that described in the metabolic syndrome and is characterized by high triglycerides and low LDL levels and gets worse with worsening renal function (Saland et al., 2019; Visconti et al., 2016). The etiology of this abnormality is often attributed to co-morbidities, such as diabetes or obesity, and it has been suggested that there is a causal relationship between dyslipidemia and progression of CKD. However, genetic mutations that lead to similar lipid profiles are not associated with the development of CKD (Lanktree et al., 2018). Patients with CKD and dyslipidemia are at high risk of cardiovascular complications, and a recent post hoc analysis of the Study of Heart and Renal Protection (SHARP) trial data has shown that high triglycerides are independently associated with worse cardiovascular outcomes (Lamprea-Montealegre et al., 2020). Our data suggest that the presence of CKD alone may generate this abnormal lipid profile, which, along with the accumulation of uremic endothelial toxins such as indoxyl sulfate, may provide insights into the close association between CKD and cardiovascular disease (Lano et al., 2020; Provenzano et al., 2019). Although we have not identified the source of the long-chain fatty acids in the sera of these mice with CKD, we have demonstrated downregulation of the catabolic pathways for the TG and DAG in the renal tissue, suggesting the kidney, rather than the liver, may be responsible for this rise in their concentration in the circulation that we found in our metabolomic studies. The kidney is one of the most important organs for the biosynthesis of myo-inositol (Croze and Soulage, 2013). Myo-inositol plays an important role in various cellular processes including as the structural basis for phosphatidylinositol formation in the plasma membrane and subsequent secondary messengers important in downstream signaling pathways, including soluble cytoplasmic inositol-1,4,5-trisphosphate (IP3) and diacylglycerol (DAG). These secondary messengers activate protein kinase C, which is known to drive oxidative stress, further mitochondrial injury and upregulation of pro-fibrotic pathways (Li et al., 2019)

In addition, we have highlighted some interesting differences in pro-fibrotic cytokines between the early and late stages of CKD. These included Eng (encoding endoglin) and *Plvap*, which were upregulated at

day 32 but downregulated at day 100. Endoglin is part of the TGF-β co-receptor complex and as such plays an important role in TGF-β signaling through SMADs, a key transduction pathway in fibrogenesis (Munoz-Felix et al., 2016; Scharpfenecker et al., 2009). *Plvap* encodes plasmalemmal vesicle-associated protein (PV-1), which is solely expressed in endothelial cells of fenestrated capillaries, such as those in the kidney. It is required for the development of fenestral diaphragms and is upregulated in vascular remodeling in the kidney, and knockout of this gene leads to hyperlipidemia and liver fibrosis (Nishi et al., 2010; Yamamoto et al., 2007).

In conclusion, we have confirmed the findings of others that AKI leads to metabolic dysfunction, inflammation, and fibrogenesis, which remain active despite maximal renal functional recovery following AKI. In addition, we have shown that, although the inflammation and fibrotic drive subside over time, the metabolic dysfunction persists and the total burden of extracellular matrix continues to increase as renal function declines as a result of progressive CKD. Alongside this is the development of dyslipidemia with raised triglycerides, which is similar to that found in the metabolic syndrome and is now recognized to be associated with the development of cardiovascular disease.

Limitations of the study

Our study does have some limitations. As an observational study, we are unable to establish cause and effect, and so, we cannot be sure that the metabolic dysfunction observed contributes to the progression of fibrosis. Although we generated transcriptomic and metabolomic data, to study global changes in gene expression and metabolism in a mouse model of nephropathy, we have not correlated these findings at the protein level in renal tissue. We used serum blood metabolomics to study the impact of observed gene expression alterations on changes in the endogenous metabolome, which we speculate are a direct effect of the induced renal disease. It is possible, however, that the renal disease has impacted the function of other tissues such as the liver and these metabolic changes are secondary to this. We hypothesize that the metabolic changes observed may lead to cardiovascular disease, but we have not investigated this in our model.

Resource availability

Lead contact

Further information, requests, and inquiries should be directed to and will be fulfilled by the Lead Contact, Claire Sharpe (claire.sharpe@kcl.ac.uk).

Data availability

The RNA-seq raw data were deposited at Sequence Read Archive with accession number: PRJNA646347. The metadata is summarized in Table S11.

Materials availability

The study did not generate new unique reagents.

METHODS

All methods can be found in the accompanying Transparent methods supplemental file.

SUPPLEMENTAL INFORMATION

Supplemental information can be found online at https://doi.org/10.1016/j.isci.2021.102046.

ACKNOWLEDGMENTS

This study was supported by Kidney UK Research (ST_003_20151126), Engineering and Physical Sciences Research Council (EPSRC) (EP/S001301/1), Biotechnology Biological Sciences Research Council (BBSRC) (BB/S016899/1), and Science for Life Laboratory (SciLifeLab). The authors would like to acknowledge the National Genomics Infrastructure (NGI) at Science for Life Laboratory for providing assistance in massive parallel sequencing. The authors acknowledge use of the research computing facility at King's College London, Rosalind (https://rosalind.kcl.ac.uk) and Swedish National Infrastructure for Computing at SNIC through Uppsala Multidisciplinary Center for Advanced Computational Science (UPPMAX) under Project SNIC 2019/3-226.

AUTHOR CONTRIBUTIONS

Conceptualization, A.H. and C.C.S.; Methodology and Investigation, A.H., S.L., and S. Saha; Software, G.B.; Formal Analysis, A.H. and G.B.; Writing – Original Draft, A.H., S. Shoaie, and C.C.S.; Writing – Review & Editing, A.H., C.C.S., S. Shoaie, and A.M.; Resources, C.C.S., S. Shoaie, and A.M.; Supervision, A.M. and B.H.

DECLARATION OF INTERESTS

The authors declare no competing interests.

Received: October 1, 2020
Revised: December 12, 2020
Accepted: January 6, 2021
Published: February 19, 2021

REFERENCES

Anders, H.J., and Schaefer, L. (2014). Beyond tissue injury-damage-associated molecular patterns, toll-like receptors, and inflammasomes also drive regeneration and fibrosis. J. Am. Soc. Nephrol. *25*, 1387–1400.

Anders, S., and Huber, W. (2010). Differential expression analysis for sequence count data. Genome Biol. *11*, R106.

Bakris, G.L., Agarwal, R., Anker, S.D., Pitt, B., Ruilope, L.M., Rossing, P., Kolkhof, P., Nowack, C., Schloemer, P., Joseph, A., et al. (2020). Effect of Finerenone on chronic kidney disease outcomes in type 2 diabetes. N. Engl. J. Med. *383*, 2219–2229.

Balzer, M.S., and Susztak, K. (2020). The interdependence of renal epithelial and endothelial metabolism and cell state. Sci. Signal. *13*, eabb8834.

Basile, D.P., Bonventre, J.V., Mehta, R., Nangaku, M., Unwin, R., Rosner, M.H., Kellum, J.A., Ronco, C., and Group, A.X.W. (2016). Progression after AKI: understanding Maladaptive repair processes to predict and identify therapeutic treatments. J. Am. Soc. Nephrol. *27*, 687–697.

Bonventre, J.V. (2014). Maladaptive proximal tubule repair: cell cycle arrest. Nephron Clin. Pract. *127*, 61–64.

Bookout, A.L., Jeong, Y., Downes, M., Yu, R.T., Evans, R.M., and Mangelsdorf, D.J. (2006). Anatomical profiling of nuclear receptor expression reveals a hierarchical transcriptional network. Cell *126*, 789–799.

Calvani, M., Benatti, P., Mancinelli, A., D'Iddio, S., Giordano, V., Koverech, A., Amato, A., and Brass, E.P. (2004). Carnitine replacement in end-stage renal disease and hemodialysis. Ann. N Y Acad. Sci. *1033*, 52–66.

Charnas, L.R., Bernardini, I., Rader, D., Hoeg, J.M., and Gahl, W.A. (1991). Clinical and laboratory findings in the oculocerebrorenal syndrome of Lowe, with special reference to growth and renal function. N. Engl. J. Med. *324*, 1318–1325.

Chegary, M., Brinke, H., Ruiter, J.P., Wijburg, F.A., Stoll, M.S., Minkler, P.E., van Weeghel, M., Schulz, H., Hoppel, C.L., Wanders, R.J., et al. (2009). Mitochondrial long chain fatty acid beta-oxidation in man and mouse. Biochim. Biophys. Acta *1791*, 806–815.

Chen, D.Q., Cao, G., Chen, H., Liu, D., Su, W., Yu, X.Y., Vaziri, N.D., Liu, X.H., Bai, X., Zhang, L., et al. (2017). Gene and protein expressions and metabolomics exhibit activated redox signaling and wnt/beta-catenin pathway are associated with metabolite dysfunction in patients with chronic kidney disease. Redox Biol. *12*, 505–521.

Chung, K.W., Dhillon, P., Huang, S., Sheng, X., Shrestha, R., Qiu, C., Kaufman, B.A., Park, J., Pei, L., Baur, J., et al. (2019). Mitochondrial damage and activation of the STING pathway lead to renal inflammation and fibrosis. Cell Metab. *30*, 784–799.e5.

Croze, M.L., and Soulage, C.O. (2013). Potential role and therapeutic interests of myo-inositol in metabolic diseases. Biochimie *95*, 1811–1827.

Fresno, C., and Fernandez, E.A. (2013). RDAVIDWebService: a versatile R interface to DAVID. Bioinformatics *29*, 2810–2811.

Guzzi, F., Cirillo, L., Roperto, R.M., Romagnani, P., and Lazzeri, E. (2019). Molecular mechanisms of the acute kidney injury to chronic kidney disease transition: an updated view. Int. J. Mol. Sci. *20*, 4941.

Heerspink, H.J.L., Stefansson, B.V., Correa-Rotter, R., Chertow, G.M., Greene, T., Hou, F.F., Mann, J.F.E., McMurray, J.J.V., Lindberg, M., Rossing, P., et al. (2020). Dapagliflozin in patients with chronic kidney disease. N. Engl. J. Med. *383*, 1436–1446.

Huang da, W., Sherman, B.T., and Lempicki, R.A. (2009). Systematic and integrative analysis of large gene lists using DAVID bioinformatics resources. Nat. Protoc. *4*, 44–57.

Jadot, I., Decleves, A.E., Nortier, J., and Caron, N. (2017). An integrated view of aristolochic acid nephropathy: update of the literature. Int. J. Mol. Sci. *18*, 297.

Jansen, G.A., Hogenhout, E.M., Ferdinandusse, S., Waterham, H.R., Ofman, R., Jakobs, C., Skjeldal, O.H., and Wanders, R.J. (2000). Human phytanoyl-CoA hydroxylase: resolution of the gene structure and the molecular basis of Refsum's disease. Hum. Mol. Genet. *9*, 1195–1200.

Kang, H.M., Ahn, S.H., Choi, P., Ko, Y.A., Han, S.H., Chinga, F., Park, A.S., Tao, J., Sharma, K., Pullman, J., et al. (2015). Defective fatty acid oxidation in renal tubular epithelial cells has a key role in kidney fibrosis development. Nat. Med. *21*, 37–46.

Kida, Y. (2020). Peritubular capillary rarefaction: an underappreciated regulator of CKD progression. Int. J. Mol. Sci. *21*, 8255.

Lamprea-Montealegre, J.A., Staplin, N., Herrington, W.G., Haynes, R., Emberson, J., Baigent, C., de Boer, I.H., and Group, S.C. (2020). Apolipoprotein B, Triglyceride-rich lipoproteins, and risk of cardiovascular events in persons with CKD. Clin. J. Am. Soc. Nephrol. *15*, 47–60.

Lanktree, M.B., Theriault, S., Walsh, M., and Pare, G. (2018). HDL cholesterol, LDL cholesterol, and triglycerides as risk factors for CKD: a mendelian randomization study. Am. J. Kidney Dis. *71*, 166–172.

Lano, G., Burtey, S., and Sallée, M. (2020). Indoxyl sulfate, a uremic endotheliotoxin. Toxins (Basel) *12*, 229.

Li, L., Wang, C., Yang, H., Liu, S., Lu, Y., Fu, P., and Liu, J. (2017). Metabolomics reveal mitochondrial and fatty acid metabolism disorders that contribute to the development of DKD in T2DM patients. Mol. Biosyst. *13*, 2392–2400.

Li, X., Xu, L., Hou, X., Geng, J., Tian, J., Liu, X., and Bai, X. (2019). Advanced oxidation protein products aggravate tubulointerstitial fibrosis through protein kinase C-dependent mitochondrial injury in early diabetic nephropathy. Antioxid. Redox Signal. *30*, 1162–1185.

Lovisa, S., Zeisberg, M., and Kalluri, R. (2016). Partial epithelial-to-mesenchymal transition and other new mechanisms of kidney fibrosis. Trends Endocrinol. Metab. *27*, 681–695.

Lu, J., Shi, J., Gui, B., Yao, G., Wang, L., Ou, Y., Zhu, D., Ma, L., Ge, H., and Fu, R. (2016). Activation of PPAR-gamma inhibits PDGF-induced proliferation of mouse renal fibroblasts. Eur. J. Pharmacol. *789*, 222–228.

Mardinoglu, A., Boren, J., Smith, U., Uhlen, M., and Nielsen, J. (2018). Systems biology in

hepatology: approaches and applications. Nat. Rev. Gastroenterol. Hepatol. *15*, 365–377.

Mardinoglu, A., and Nielsen, J. (2015). New paradigms for metabolic modeling of human cells. Curr. Opin. Biotechnol. *34*, 91–97.

Mardinoglu, A., Shoaie, S., Bergentall, M., Ghaffari, P., Zhang, C., Larsson, E., Backhed, F., and Nielsen, J. (2015). The gut microbiota modulates host amino acid and glutathione metabolism in mice. Mol. Syst. Biol. *11*, 834.

Marx, D., Metzger, J., Pejchinovski, M., Gil, R.B., Frantzi, M., Latosinska, A., Belczacka, I., Heinzmann, S.S., Husi, H., Zoidakis, J., et al. (2018). Proteomics and metabolomics for AKI diagnosis. Semin. Nephrol. *38*, 63–87.

Mizuno, Y., Ninomiya, Y., Nakachi, Y., Iseki, M., Iwasa, H., Akita, M., Tsukui, T., Shimozawa, N., Ito, C., Toshimori, K., et al. (2013). Tysnd1 deficiency in mice interferes with the peroxisomal localization of PTS2 enzymes, causing lipid metabolic abnormalities and male infertility. PLoS Genet. *9*, e1003286.

Munoz-Felix, J.M., Perez-Roque, L., Nunez-Gomez, E., Oujo, B., Arevalo, M., Ruiz-Remolina, L., Cuesta, C., Langa, C., Perez-Barriocanal, F., Bernabeu, C., et al. (2016). Overexpression of the short endoglin isoform reduces renal fibrosis and inflammation after unilateral ureteral obstruction. Biochim. Biophys. Acta *1862*, 1801–1814.

Nishi, Y., Namikoshi, T., Sasaki, T., Tokura, T., Nagasu, H., Nakanishi, H., Kozuka, Y., and Kashihara, N. (2010). Histopathological manifestations of membranoproliferative glomerulonephritis and glomerular expression of plasmalemmal vesicle-associated protein-1 in a patient with polycythemia vera. Clin. Nephrol. *74*, 393–398.

O'Brien, E.J., Monk, J.M., and Palsson, B.O. (2015). Using genome-scale models to predict biological capabilities. Cell *161*, 971–987.

Ohashi, R., Shimizu, A., Masuda, Y., Kitamura, H., Ishizaki, M., Sugisaki, Y., and Yamanaka, N. (2002). Peritubular capillary regression during the progression of experimental obstructive nephropathy. J. Am. Soc. Nephrol. *13*, 1795–1805.

Orth, J.D., Thiele, I., and Palsson, B.O. (2010). What is flux balance analysis? Nat. Biotechnol. *28*, 245–248.

Ortiz, A., Sanchez-Nino, M.D., Izquierdo, M.C., Martin-Cleary, C., Garcia-Bermejo, L., Moreno, J.A., Ruiz-Ortega, M., Draibe, J., Cruzado, J.M., Garcia-Gonzalez, M.A., et al. (2015). Translational value of animal models of kidney failure. Eur. J. Pharmacol. *759*, 205–220.

Padovano, V., Podrini, C., Boletta, A., and Caplan, M.J. (2018). Metabolism and mitochondria in polycystic kidney disease research and therapy. Nat. Rev. Nephrol. *14*, 678–687.

Park, J., Shrestha, R., Qiu, C., Kondo, A., Huang, S., Werth, M., Li, M., Barasch, J., and Suszták, K. (2018). Single-cell transcriptomics of the mouse kidney reveals potential cellular targets of kidney disease. Science *360*, 758–763.

Perkovic, V., Jardine, M.J., Neal, B., Bompoint, S., Heerspink, H.J.L., Charytan, D.M., Edwards, R., Agarwal, R., Bakris, G., Bull, S., et al. (2019). Canagliflozin and renal outcomes in type 2 diabetes and nephropathy. N. Engl. J. Med. *380*, 2295–2306.

Podrini, C., Rowe, I., Pagliarini, R., Costa, A.S.H., Chiaravalli, M., Di Meo, I., Kim, H., Distefano, G., Tiranti, V., Qian, F., et al. (2018). Dissection of metabolic reprogramming in polycystic kidney disease reveals coordinated rewiring of bioenergetic pathways. Commun. Biol. *1*, 194.

Provenzano, M., Coppolino, G., De Nicola, L., Serra, R., Garofalo, C., Andreucci, M., and Bolignano, D. (2019). Unraveling cardiovascular risk in renal patients: a new take on old tale. Front. Cell Dev. Biol. *7*, 314.

Reinecke, F., Smeitink, J.A., and van der Westhuizen, F.H. (2009). OXPHOS gene expression and control in mitochondrial disorders. Biochim. Biophys. Acta *1792*, 1113–1121.

Reis, A., Rudnitskaya, A., Chariyavilaskul, P., Dhaun, N., Melville, V., Goddard, J., Webb, D.J., Pitt, A.R., and Spickett, C.M. (2015). Top-down lipidomics of low density lipoprotein reveal altered lipid profiles in advanced chronic kidney disease. J. Lipid Res. *56*, 413–422.

Rhee, E.P., Clish, C.B., Ghorbani, A., Larson, M.G., Elmariah, S., McCabe, E., Yang, Q., Cheng, S., Pierce, K., Deik, A., et al. (2013). A combined epidemiologic and metabolomic approach improves CKD prediction. J. Am. Soc. Nephrol. *24*, 1330–1338.

Rowe, I., Chiaravalli, M., Mannella, V., Ulisse, V., Quilici, G., Pema, M., Song, X.W., Xu, H., Mari, S., Qian, F., et al. (2013). Defective glucose metabolism in polycystic kidney disease identifies a new therapeutic strategy. Nat. Med. *19*, 488–493.

Saland, J.M., Kupferman, J.C., Pierce, C.B., Flynn, J.T., Mitsnefes, M.M., Warady, B.A., and Furth, S.L. (2019). Change in dyslipidemia with declining glomerular filtration rate and increasing proteinuria in children with CKD. Clin. J. Am. Soc. Nephrol. *14*, 1711–1718.

Scarpulla, R.C. (2008). Transcriptional paradigms in mammalian mitochondrial biogenesis and function. Physiol. Rev. *88*, 611–638.

Scharpfenecker, M., Floot, B., Russell, N.S., Ten Dijke, P., and Stewart, F.A. (2009). Endoglin haploinsufficiency reduces radiation-induced fibrosis and telangiectasia formation in mouse kidneys. Radiother. Oncol. *92*, 484–491.

Smith, C.L., Blake, J.A., Kadin, J.A., Richardson, J.E., Bult, C.J., and Mouse Genome Database Group. (2018). Mouse Genome Database (MGD)-2018: knowledgebase for the laboratory mouse. Nucleic Acids Res. *46*, D836–D842.

Tan, X., Cao, X., Zou, J., Shen, B., Zhang, X., Liu, Z., Lv, W., Teng, J., and Ding, X. (2017). Indoxyl sulfate, a valuable biomarker in chronic kidney disease and dialysis. Hemodial Int. *21*, 161–167.

Varanasi, U., Chu, R., Chu, S., Espinosa, R., LeBeau, M.M., and Reddy, J.K. (1994). Isolation of the human peroxisomal acyl-CoA oxidase gene: organization, promoter analysis, and chromosomal localization. Proc. Natl. Acad. Sci. U S A *91*, 3107–3111.

Visconti, L., Benvenga, S., Lacquaniti, A., Cernaro, V., Bruzzese, A., Conti, G., Buemi, M., and Santoro, D. (2016). Lipid disorders in patients with renal failure: role in cardiovascular events and progression of chronic kidney disease. J. Clin. Transl. Endocrinol. *6*, 8–14.

Walkin, L., Herrick, S.E., Summers, A., Brenchley, P.E., Hoff, C.M., Korstanje, R., and Margetts, P.J. (2013). The role of mouse strain differences in the susceptibility to fibrosis: a systematic review. Fibrogenesis Tissue Repair *6*, 18.

Yamamoto, I., Horita, S., Takahashi, T., Tanabe, K., Fuchinoue, S., Teraoka, S., Hattori, M., and Yamaguchi, Y. (2007). Glomerular expression of plasmalemmal vesicle-associated protein-1 in patients with transplant glomerulopathy. Am. J. Transplant *7*, 1954–1960.

Zeisberg, M., and Neilson, E.G. (2010). Mechanisms of tubulointerstitial fibrosis. J. Am. Soc. Nephrol. *21*, 1819–1834.

iScience, Volume *24*

Supplemental Information

Acute kidney injury leading to CKD is associated with a persistence of metabolic dysfunction and hypertriglyceridemia

Azadeh Harzandi, Sunjae Lee, Gholamreza Bidkhori, Sujit Saha, Bruce M. Hendry, Adil Mardinoglu, Saeed Shoaie, and Claire C. Sharpe

Supplemental information

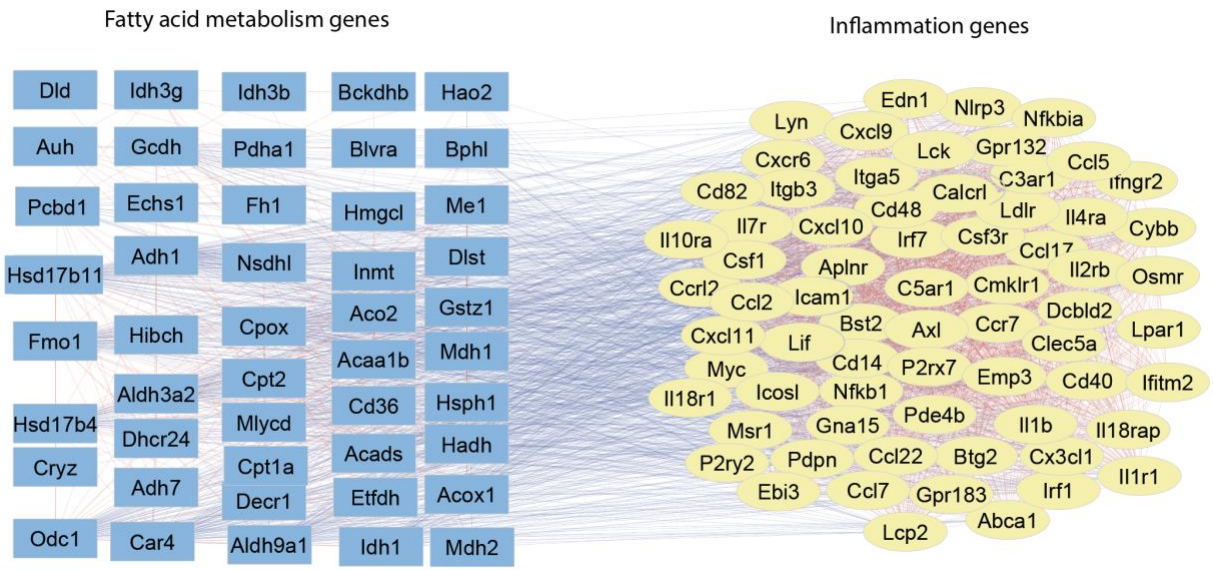

Figure S1, related to Figure 2G. Correlation between inflammation and fatty acid metabolism. The blue lines demonstrate negative correlation between downregulated fatty acid metabolism genes (blue) and upregulated inflammation genes (yellow) (Spearman's rank-order correlation analysis).

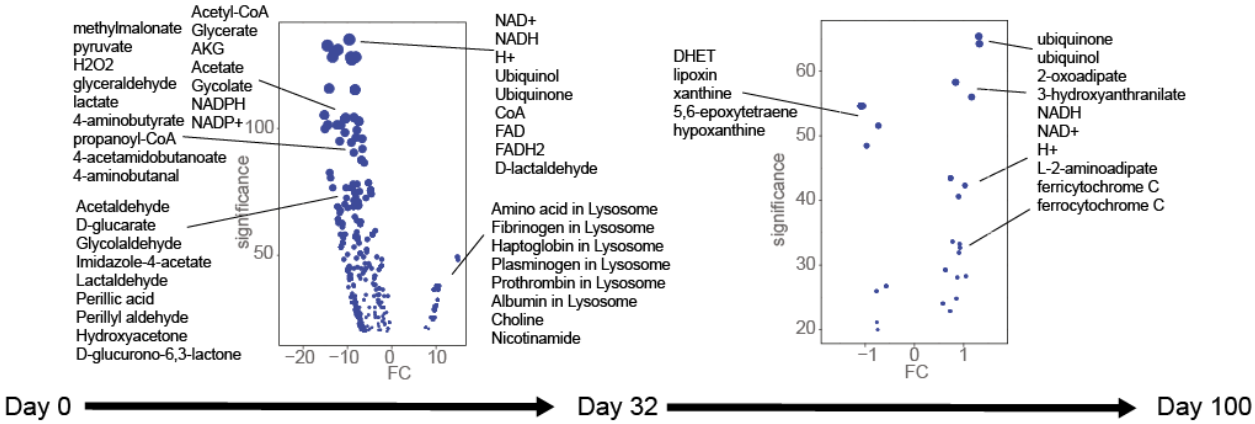

Figure S2, related to Figure 3. The reporter metabolite analysis outcome is summarized in the volcano plots from baseline to Day 100. The data from the reporter metabolite analysis suggesting mitochondrial dysfunction in early CKD (Day 32) with some improvement by Day 100.

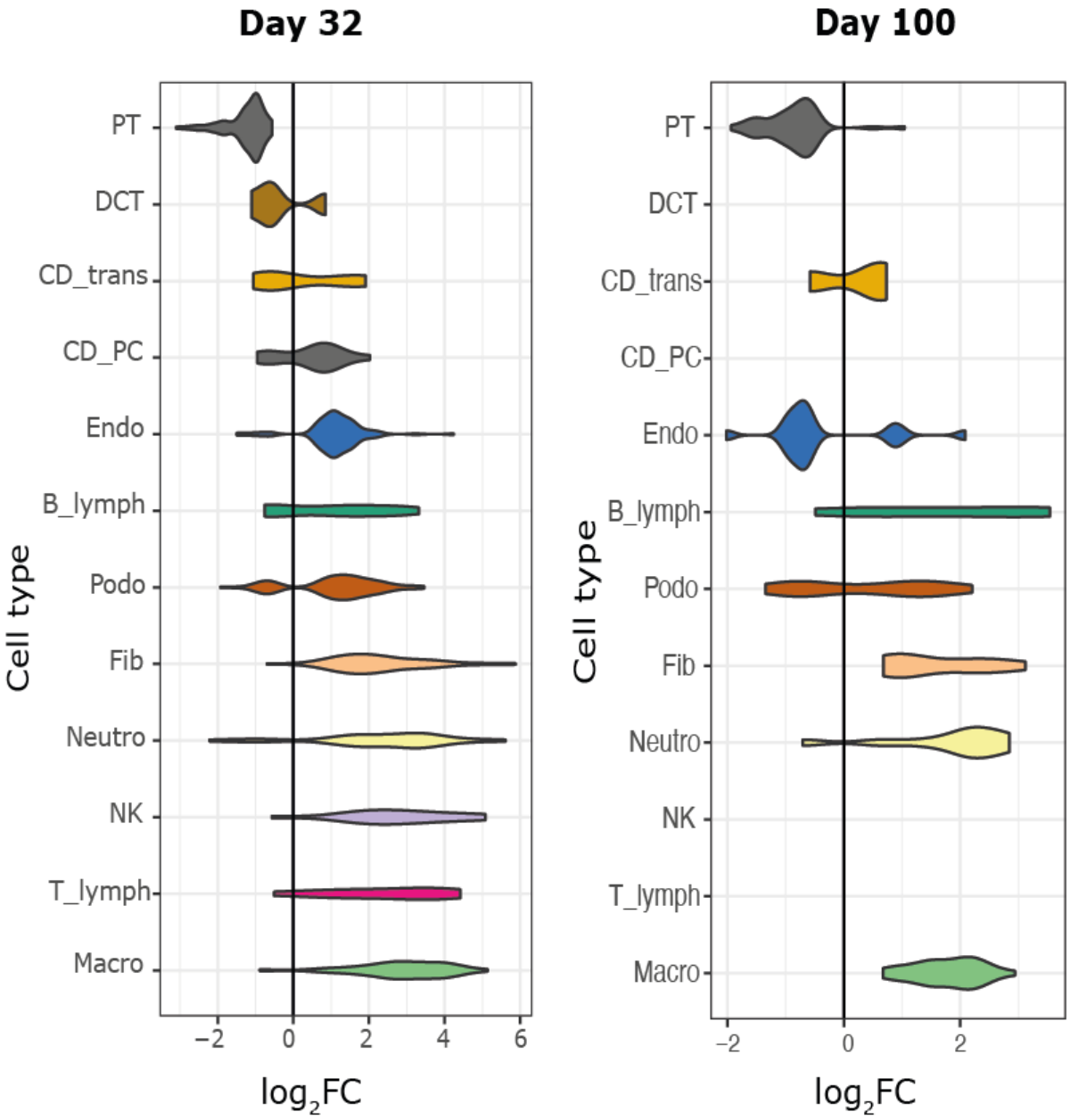

Figure S3, related to Figure 6 and Table S 7. Cell-specific expression changes at days 32 and 100 based on cell type markers derived from published mouse kidney single cell transcriptomics. At day 32 downregulation of proximal tubule cell marker gene expression is considerable, whilst cell marker expression of macrophages, T lymphocytes, neutrophils, and fibroblasts is extensively upregulated. These changes are still apparent at day 100.

A

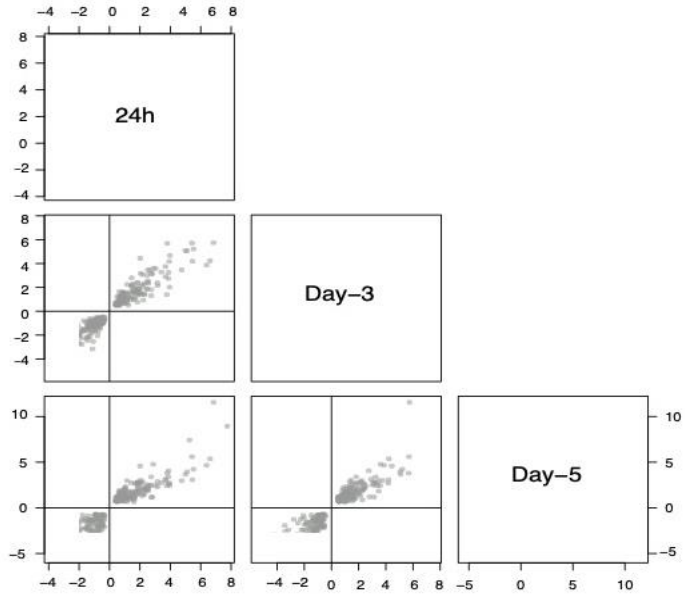

B

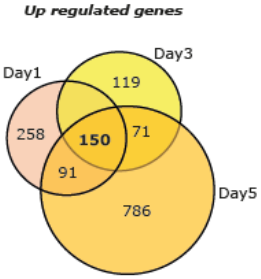

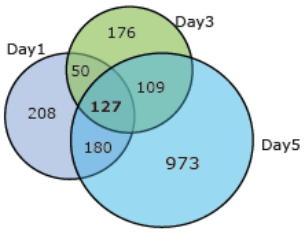

C

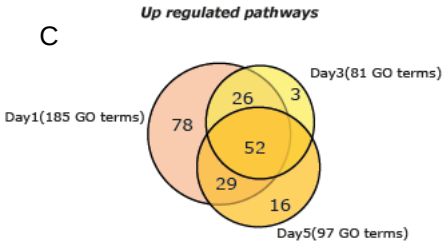

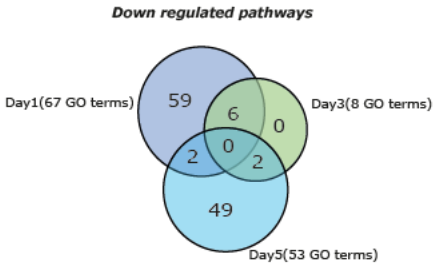

Figure S4, related to Figure 6. A) Scatter plots showing the variation comparison of genes which are similarly differentially significantly expressed at all time points in two different groups. axis=y is an indicator of one group and axis=x is indicator of different group with value of log fold change 2 for each gene. B) Venn diagram showing the numbers of shared significantly up/down-regulated genes at each time point. C) Venn diagram showing the numbers of shared enriched pathways of up/down-regulated genes at each time point (FDR < 0.05).

Gene	Cat nr	Target species	Taq-Man search
Acta2, alpha-SMA	4331182	Mouse	Mm01546133_m1
Gapdh	4331182	Mouse	Mm99999915_g1

Table S10. Related to Figure 5. List of TaqMan probes for primers using in RT-qPCR for *in-vitro* model

Transparent Methods

Aristolochic Acid Nephropathy (AAN) Murine model establishment and sample collection

All the experimental procedures were approved under provisions of the animals (Scientific Procedures) Act 1986 and were performed under license number PPL 70/8665. We used male CD1 mice (8 weeks old) for this study. Aristolochic acid (AA) isoform I (Sigma, A9451, Solvent: Normal Saline) with a dose of 3.5mg/kg was administered through an intra-peritoneal injection on day 1 and on day 5. Normal saline was administrated on day 1 and day 5 to control mice. We sacrificed mice at three time points (days 0, 32 and 100) after the first AA injection.

Mouse Proximal Tubular Epithelial cell-line (MPTEC)

Mouse proximal tubule epithelial cells were obtained from Dr Mark Dockrell South West Thames Institute for Renal Research. This cell line was isolated from the S3 segment of the proximal tubule, a Brinster transgenic mouse carries the T antigen of SV40 virus that makes the cells immortalized.

Mouse proximal tubular epithelial (MPTE) cell line model of epithelial to mesenchymal transition

6×10^6 MPTE cells were seeded in 6-well plates. After 24 hours they were treated with 10 ng/μl TGF-β and Epidermal Growth Factor (EGF) as previously described (Hutchison et al., 2009). RNA was extracted from cells after 24 hours, 3 days and 5 days.

For MPTE cell line medium we used DMEM/F12 (1:1) medium (Life Technologies) supplemented with Hydrocortisone (50nM), Penicillin-Streptomycin, 1% Insulin Transferrin Selinate (ITS) (Gibco, Life Technologies) and 1%Fetal Calf Serum (FCS).

Renal Functional assays for serum Creatinine and Blood Urea Nitrogen (BUN)

0.2ml/40g mouse blood was collected from live mice or via cardiac puncture at the point of sacrifice. Clotted blood samples were centrifuged at 4000 rpm for 10min to obtain the serum. Serum creatinine measurement was performed using an enzymatic assay, from Crystal Chem using a mouse creatinine assay kit (#80350). Each sample was analyzed in triplicate and a technical mean calculated. The Max Discovery Blood Urea Nitrogen Enzymatic Kit (Bio scientific #5602-01) provided all the reagents and standards required for the assay. Each sample was analysed in triplicate and a technical mean calculated.

Histology and Picro Sirius Red staining

Half of each kidney was formalin-fixed, and paraffin embedded. 4 μm sections were cut and stained with Picro Sirius red (PSR) for 2 hours. A Nikon Eclipse TE2000-S light microscope was used for imaging and quantification of the Picro Sirius Red staining (collagen) was performed using NIS Elements Basic Research Software.

Hydroxyproline Assay

The QuickZyme Total Collagen assay from QuickZyme Biosciences (QZBtiscol1) was used to measure the concentration of Hydroxyproline in the murine samples. Tissue samples (300g) were mixed with 6M hydrochloride acid (100mg/ml). Mixed samples were heated at 95°C for 20 hours followed by cooling at room temperature and centrifuging for 10 minutes at 13,000 g. The supernatant of the hydrolysed samples and standards were removed and diluted in distilled water. Hydrolysed sample/standard was added into pre-determined wells in duplicates followed by adding assay buffer for 20 minutes at room temperature and second buffer addition for 60 minutes incubation at 60°C. The hydroxyproline concentration (µg/ml) was read in a spectrophotometer at 570nm.

Mouse serum blood sampling and storage for metabolomics

Cardiac puncture was performed when mice were being sacrificed for collecting the kidney. 1ml insulin syringe with 23G needle were used to aspirate of all available blood. Obtained blood was centrifuged for 10 min at 4000 rpm (4°C) and supernatant were collected and stored at -80°C for future use.

Western blot and quantification

Cells were lysed with RIPA buffer from Sigma with added protease inhibitor cocktail (Roche). Protein samples underwent electrophoretic separation on an 8% SDS–PAGE gel and were transferred onto nitrocellulose membranes for 2 hours at 60 voltage. Membranes were blocked for one hour in 5% skimmed milk in TBST (Tris-buffered saline, 0.1% Tween 20) then incubated in primary antibodies (E-cadherin antibody 1:1000 dilution from BD (610181)) over night at 4°C followed by TBST washing and exposure to secondary Rabbit anti-mouse HRP 1:15000 (from DAKO catalogue number: P0260) for 1h in room temperature dark box. GAPDH antibody from Cell Signalling was used (2118L) to quantify this housekeeping protein, secondary antibody LI-COR. Visualization of protein in the membrane was achieved using a LI-COR machine. The density of protein expression was measured by Image Studio Lite, a densitometry software from LI-COR to compare the density of expressed protein in each condition ratioed to GAPDH.

Immunocytochemistry

MPTE cells were grown on coverslips to 80% confluency, washed with PBS, fixed for 10 minutes with 4% paraformaldehyde then permeabilized with PBS containing 0.25% Triton X-100. Cells were then blocked for 1h in 1% BSA (bovine serum albumin) in PBST (Phosphate Buffered Saline + Tween 20). Fixed cells were incubated in primary antibody (E-cadherin dilution of 1:500) overnight at 4°C humidity chamber. Alexa flour 488 (Thermofisher, A-11001) were used for E-cad as a secondary antibody at room temperature and cell nuclei were stained with Hoechst for 2min. All slides were mounted with mounting medium (VECTOR Cat. No H-1000) and images were produced with Confocal microscope (Leica SP5, Germany) at ×40 magnification.

Immunofluorescence for staining Filamentous actin (F-actin)

After fixation for 10 minutes in fixation buffer from Biolegend (Cat No. 42080) and permeabilization with 0.1% Triton X-100, cells were blocked with 1% BSA. Rhodamine phalloidin (Thermofisher, R415) was used for 30 minutes at room temperature for F-actin staining. The wavelength range for excitation and emission was 540/565 nm.

Cell line RNA isolation

An RNaesy mini kit (Cat No./ID: 74104, Qiagen) was used for total RNA extraction from cells. After cell disruption with the lysis buffer plus beta-mercaptoethanol (β-ME) to prevent RNA degradation, homogenization with QIAshredder spin column was followed by washing and DNase Max kit from Qiagen to remove contaminating genomic DNA according to the manufacture's protocol.

Mouse tissue RNA isolation

A TissueLyser ll machine (Qiagen #85300) was used to disrupt and homogenise the small piece of kidney tissue using 1 ml TRIZOL (Ambion, #15596-018) in 2 ml rounded bottom tube and 1 stainless steel bead (5 mm, Qiagen, # 69989). Homogenised samples were centrifuged for 5min at 1000g and supernatants were transferred into new tubes. 200μl chloroform was added into each sample tube and vortexed vigorously for 10 minutes and again incubated for 2 min at room temperature. Samples were then centrifuged for 15 min at 12,000g (at 4°C) and the upper phase were transferred into new 1.5ml tubes with 500μl of isopropanol and incubated at room temperature for 10min. After which, all samples were centrifuged again at 12,000g (at 4°C) and supernatants were discarded. Samples were washed with 900μl of 70% Ethanol and centrifuged at 7,400g (at 4ºC) and air-dried for 10 minutes. pellets were resuspended in 20μl of DEPC treated water and stored at -80 ºC.

Quality measurement of RNA

After extracting RNA from samples (tissue and cell line), for quality control the RNA integrity number (RIN) was measured using the Agilent Biolanalyzer RNA 6000 Nano assay. This number can be between 1 to 10, the higher number the better quality of RNA. The sequencing platform we used required the RIN number to be not less than 8.

Quantitative Real Time PCR (qRT-PCR)

Complementary DNA (cDNA) was synthesized from 1μg RNA using High-capacity RNA-to-cDNA Kit (ThermoFisher,4387406). Quantitative RT-PCR was performed with 1:1 template cDNA with 1:5 dilution, followed by TaqMan universal PCR Master Mix (Life technology) and 1μl of TaqMan probe primer in 20μl final volume for each reaction. Real-time PCR was performed in triplicate using a QuanStudio 7 Flex Real time PCR system, ThermoFisher. GAPDH was used as an internal control gene for the relative expression levels performed by $2^{-\Delta\Delta Ct}$ method. The TaqMan probe Catalog numbers are in Table S10.

Transcript profiling of mouse tissues and cell lines

Total RNA was extracted from mouse tissues and cell lines and their library were prepared using Illumina TruSeq with poly-A selection and sequenced by Illumina NovaSeq 6000 sequencing system (2 x 50bp). Quality of raw data was checked with *FastQC* (http://www.bioinformatics.babraham.ac.uk/projects/fastqc) and processed with *Kallisto* (Bray et al., 2016) with mouse reference genome (GENCODE database ver. M17)(Frankish et al., 2019), quantifying Transcript per million (TPM) and raw read counts. Processed RNA-seq was benchmarked with STAR aligner (Dobin et al., 2013) and HT-seq (Anders et al., 2015) quantification program. Raw read counts were analyzed for differential expression analysis, performed by negative binomial tests of R DESeq package (Anders and Huber, 2010). Enriched gene ontology/pathways of DEGs were analyzed with R RDAVID Web Service package.

Genome-scale metabolic modelling of mouse model

The maximum TPM of the expression data were used to make a generic kidney expression profile and integrated into MMR model to construct generic kidney genome scale metabolic model (GEM) using tINIT (Agren et al., 2012). Gene levels in tINIT were considered based on the TPM value; no expression (TPM<1), low (1≤TPM<10), and medium-high (TPM≥10). We considered maximization ATP consumption and biomass production as objective functions for the generic model. We used MADE to generate specific GEMs using fold changes and adjusted p-value obtained through DESeq, generic kidney GEM and TIGER (Bidkhori et al., 2018; Jensen et al., 2011) and Gurobi solver was used for the flux balance approach. Reporter metabolite analysis (Patil and Nielsen, 2005) was performed through PIANO (Varemo et al., 2013) using fold changes and adjusted p-value obtained through DESeq, with geneSetStat = reporter and number of Permutation = 1000 by function *runGSA*. For the interpretation, the metabolites significantly changed with clear direction were considered (FDR<0.01).

Metabolomics

Biocrates' info: All samples were stored immediately upon receipt at -80 °C for measuring metabolite concentrations in mouse serum samples. A mass spectrometry-based metabolomics approach was performed to determine the concentration of endogenous metabolites of various biochemical classes in these samples. Biocrates' commercially available MxP® Quant 500 kit was used for the quantification of several endogenous metabolites of various biochemical classes. Lipids and hexoses were measured by flow injection analysis-tandem mass spectrometry (FIA-MS/MS) using a 5500 QTRAP® instrument (AB Sciex, Darmstadt, Germany) with an electrospray ionization (ESI) source, and small molecules were measured by liquid chromatography-tandem mass spectrometry (LC-MS/MS) using the same 5500 QTRAP® instrument. Validated analytical methods were used for sample analysis. Absolute concentrations in mouse serum samples were obtained for metabolites from various biochemical classes. Wilcoxon signed rank test was used to compare the concentration of serum metabolites between the conditions. Sparse Partial Least Square-Discriminant Analysis (sPLS-DA) as a supervised classification method was used for serum metabolites using "mixOmics" R package (Rohart et al., 2017) and the first two components was considered for extracting the features.

Statistics

To calculate the adjusted *p-value* and control the false discovery rate (FDR) in our data we used the Benjamini-Hochberg method based on the FDR. We used an adjusted *p-value* less than 0.05 for comparing each group treatment to its age-matched controls (differentially expressed genes) in tissue samples, and for cell-line models we used an adjusted *p-value* less than 1e-5. For comparing two data sets to infer statistically significant differences, we used the Student T-test method (*p-value* < 0.05). We used the ANOVA test for multiple experimental groups and controls (more than two variables). Permutational multivariate analysis of variance (PERMANOVA) was used to check and partition dissimilarities between two or more groups using multivariate factors. For principal component analysis (PCA) plots, we used PC1 and PC2 as features of PERMANOVA to distinguish time-wise differences and treatment-wise differences. We used the Wilcoxon test as non-parametric statistical test for our metabolomics data to compare metabolites from disease AAN serum with age-matched control serum mice with a *p-value* less than 0.05. Partial least squares discriminant analysis (PLS-DA) was used for further investigation and feature selection to see how metabolites from mice at different treatment times were distinct from their age-matched controls and what features or metabolites were the cause of this separation or discrimination between clusters.

Data and Code Availability

The accession number for the RNA-seq raw data reported in this paper is Sequence Read Archive :PRJNA646347.

Supplemental References

Agren, R., Bordel, S., Mardinoglu, A., Pornputtapong, N., Nookaew, I., and Nielsen, J. (2012). Reconstruction of genome-scale active metabolic networks for 69 human cell types and 16 cancer types using INIT. PLoS Comput Biol *8*, e1002518.

Anders, S., and Huber, W. (2010). Differential expression analysis for sequence count data. Genome Biol *11*.

Anders, S., Pyl, P.T., and Huber, W. (2015). HTSeq-a Python framework to work with high-throughput sequencing data. Bioinformatics *31*, 166-169.

Bidkhori, G., Benfeitas, R., Klevstig, M., Zhang, C., Nielsen, J., Uhlen, M., Boren, J., and Mardinoglu, A. (2018). Metabolic network-based stratification of hepatocellular carcinoma reveals three distinct tumor subtypes. Proc Natl Acad Sci U S A *115*, E11874-E11883.

Bray, N.L., Pimentel, H., Melsted, P., and Pachter, L. (2016). Near-optimal probabilistic RNA-seq quantification (vol 34, pg 525, 2016). Nat Biotechnol *34*, 888-888.

Dobin, A., Davis, C.A., Schlesinger, F., Drenkow, J., Zaleski, C., Jha, S., Batut, P., Chaisson, M., and Gingeras, T.R. (2013). STAR: ultrafast universal RNA-seq aligner. Bioinformatics *29*, 15-21.

Frankish, A., Diekhans, M., Ferreira, A.M., Johnson, R., Jungreis, I., Loveland, J., Mudge, J.M., Sisu, C., Wright, J., Armstrong, J.*, et al.* (2019). GENCODE reference annotation for the human and mouse genomes. Nucleic Acids Res *47*, D766-D773.

Hutchison, N., Hendry, B.M., and Sharpe, C.C. (2009). Rho isoforms have distinct and specific functions in the process of epithelial to mesenchymal transition in renal proximal tubular cells. Cell Signal *21*, 1522-1531.

Jensen, P.A., Lutz, K.A., and Papin, J.A. (2011). TIGER: Toolbox for integrating genome-scale metabolic models, expression data, and transcriptional regulatory networks. BMC Syst Biol *5*, 147.

Patil, K.R., and Nielsen, J. (2005). Uncovering transcriptional regulation of metabolism by using metabolic network topology. Proc Natl Acad Sci U S A *102*, 2685-2689.

Rohart, F., Gautier, B., Singh, A., and Le Cao, K.A. (2017). mixOmics: An R package for 'omics feature selection and multiple data integration. PLoS Comput Biol *13*, e1005752.

Varemo, L., Nielsen, J., and Nookaew, I. (2013). Enriching the gene set analysis of genome-wide data by incorporating directionality of gene expression and combining statistical hypotheses and methods. Nucleic Acids Res *41*, 4378-4391.